AIAA JOURNAL
Vol. 52, No. 12, December 2014

Numerical Study of Hypersonic Boundary-Layer Receptivity with Freestream Hotspot Perturbations

Yuet Huang* and Xiaolin Zhong†
University of California, Los Angeles, California 90095

DOI: 10.2514/1.J052657

This paper presents a numerical-simulation study of transient flow over a blunt compression cone under the effect of freestream hotspot perturbations. This study is motivated by concurrent wind-tunnel laser-spot experiments carried out at Purdue University. The flow conditions used in the simulation are based on the experimental conditions. The simulation is performed using a high-order shock-fitting finite-difference scheme. The simulation results show that the hotspot is able to excite second-mode instability, where the instability growth is found to be dominant in the boundary layer. The receptivity mechanism is investigated by comparing the simulated results with linear-stability theory. Fast acoustic waves generated by hotspot–shock interaction excite the boundary-layer disturbances. Also, the synchronization of mode F and mode S leads to the dominance of boundary-layer disturbances by the growing second mode.

Nomenclature

a	=	phase speed
c_v	=	specific heat in a constant-volume process
$d(\,)$	=	perturbation of a variable
e	=	total energy per unit volume
F	=	frequency
F_j	=	inviscid flux vector in jth direction
F_{vj}	=	viscous flux vector in jth direction
H^*	=	local height from the wall
L^*	=	length scale of the boundary-layer thickness
M_∞	=	freestream Mach number
P	=	pressure
P_∞	=	freestream pressure
Pr	=	Prandtl number
q_j	=	heat flux due to thermal conduction
R	=	local Reynolds number
R^*	=	gas constant
Re^*_∞	=	freestream Reynolds number per unit length
S	=	entropy
S_∞	=	freestream entropy
s	=	natural coordinate along the body surface
T	=	temperature
T_o	=	total temperature
T_r	=	reference temperature
T_s	=	Sutherland's temperature
T_{wall}	=	temperature at wall
T_∞	=	freestream temperature
t	=	time
u_1, u_2, u_3	=	velocity components
u_∞	=	freestream velocity
y_n	=	normalized local normal distance from the wall
α	=	streamwise complex wave number
α_i	=	local growth rate
α_r	=	local wave number
γ	=	ratio of specific heat
ζ	=	coordinate in azimuthal direction
η	=	coordinate in the direction normal to the wall
κ	=	heat conductivity coefficient
μ	=	viscosity coefficient
μ_∞	=	freestream viscosity coefficient
μ_r	=	reference viscosity coefficient
ξ	=	coordinate in streamwise direction
ρ	=	mass density
ρ_∞	=	freestream density
τ	=	time in computational domain
τ_{ij}	=	shear-stress tensor
φ	=	phase angle
ω	=	circular frequency

Superscripts

$*$	=	dimensional variable
$'$	=	perturbation of a variable

I. Introduction

IN THE process of designing the aerodynamic and heat protection configurations of hypersonic aerospace vehicles, accurate prediction of the boundary-layer laminar–turbulent transition location on the body surface is very important. To predict the transition location accurately, the fundamental mechanisms underlying the transition process must be understood. Despite many decades of research, the mechanisms of hypersonic laminar–turbulent transition are still not well understood.

In general, the process of laminar–turbulent transition with weak freestream forcing can be divided into three stages: 1) boundary-layer receptivity, 2) linear eigenmode growth and interactions, and 3) nonlinear breakdown to turbulence. Boundary-layer receptivity is the first stage. It is the process where disturbances enter the boundary layer and generate instability waves that contain eigenmodes. After receptivity, the eigenmodes in the waves grow linearly. When the waves reach certain amplitudes and become nonlinear, they cause breakdown to turbulence. Mack showed that the second mode is the dominant instability which leads to transition when boundary-layer edge Mach numbers are approximately higher than 4 [1,2]. Therefore, the boundary-layer receptivity of linear disturbance waves and the development of second-mode instability in a boundary layer are particularly important to the study of hypersonic boundary-layer transition.

Kovasznay [3] stated that weak disturbances in compressible flow can be categorized into acoustic, entropy and vorticity disturbances. It was found that, regardless of the type of freestream disturbances hitting the shock, acoustic, entropy, and vorticity disturbances would

Received 18 April 2013; revision received 14 June 2014; accepted for publication 16 July 2014; published online 21 October 2014.

*Doctorate Student, Mechanical and Aerospace Engineering Department. Student Member AIAA.

†Professor, Mechanical and Aerospace Engineering Department. Associate Fellow AIAA.

always be generated behind the shock by the interaction between the freestream disturbances and the shock [4]. However, the mechanisms of the interaction of various types of freestream disturbances with the shock are different, which leads to the difference in wave angles and amplitudes of the generated disturbances. Thus, detailed boundary-layer receptivity studies for all three types of freestream disturbances are necessary for obtaining a complete picture of hypersonic boundary-layer receptivity.

Studies of hypersonic boundary-layer receptivity to freestream acoustic disturbances have been conducted by many researchers. For instance, the numerical studies of boundary-layer receptivity over blunt cones by Zhong and Ma [5] and Balakumar and Kegerise [6,7], the numerical studies over flat plates by Ma and Zhong [8,9], the theoretical studies on flat plates by Fedorov [10], and the experimental studies on flat plates by Maslov et al. [11].

In addition to the receptivity studies with freestream acoustic disturbances, those with freestream entropy disturbances are still at the initial stage. Schmisseur et al. [12,13] studied the receptivity of a freestream laser spot over an elliptical cone in a Mach 4 flow. Salyer et al. [14,15] characterized the laser-generated hotspot and used it in a boundary-layer receptivity experiment for a hemisphere–cylinder model in Mach 4 freestream. The schematic explanation of the laser-spot and cone setup in the experimental studies is demonstrated in Fig. 1 [12,13]. The hotspot is initially generated at a location upstream from the cone on the centerline. Then, the spot moves along with the hypersonic freestream toward the cone nose, interacts with and passes through the bow shock, and eventually travels further downstream around the cone. Schmisseur et al. [12,13] and Salyer et al. [14,15] completed benchmark tests for generating laser spots in their wind tunnel, and they measured the responses of the perturbed boundary layers. However, there was no detailed analysis of the receptivity mechanisms in their work.

Wheaton et al. [16] performed both numerical analysis and experimental instability measurements on compression cones. In their numerical analysis, they used the STABL software [17] to compute the steady base flow around compression cones in a Mach 6 freestream and to analyze the linear stability of the boundary layer. Their linear-stability theory (LST) results indicated a maximum N-factor of 16 at the aft end ($x^* \approx 0.45$ m) of the compression cone. In their Mach 6 wind-tunnel experiments, they measured the second-mode instability under quiet and noisy flows. The experimental second-mode peak frequency under quiet flow conditions with a stagnation pressure of 140 psia was 290 kHz at $x^* = 0.4$ m. Chou et al. [18] calibrated their laser-spot-generation apparatus and conducted laser-spot benchmark tests in a Mach 6 wind tunnel (BAM6QT).

Ma and Zhong [8,9] performed numerical-simulation studies on a flat plate with freestream planar sinusoidal fast acoustic, slow acoustic, entropy, and vorticity waves, and an acoustic wave beam at Mach 4.5. From their receptivity study of freestream entropy waves, the induced boundary-layer disturbances upstream contain relatively strong stable mode I first. The unstable second-mode waves are then converted from mode I by their synchronization. The induced disturbances have very strong modulations at the locations between the leading edge and the synchronization point. However, the disturbances have weak modulations at the locations near the synchronization point. From their receptivity study of freestream fast acoustic waves, the induced boundary-layer disturbances upstream contains relatively strong mode I, and the modulations are not strong there. However, the induced disturbances have very strong modulations near the synchronization point. The disturbances are dominated by mode II behind the synchronization point. Therefore, the receptivity path is different between the case of freestream entropy waves and the one of freestream fast acoustic waves. Ma and Zhong [8,9] also found that, when the acoustic waves (which are generated from freestream entropy perturbations and shock interaction) reached the boundary layer, the perturbed boundary layer would reflect the acoustic waves, and these waves would interact with the shock. These secondary acoustic waves and shock interaction would generate additional acoustic, entropy, and vorticity disturbances. When these additional disturbances combined with the initial disturbances, they would produce strong effects on the boundary-layer receptivity.

Zhong and Ma [5] performed a numerical study over a blunt cone with fast acoustic waves in a Mach 7.99 freestream. In their study, the induced boundary-layer disturbances contain relatively strong mode I at the locations shortly behind the nose region. The relatively strong components in the waves switch to fast acoustic waves in the middle region of the cone. The modulations are strong at locations between the nose region and the synchronization point. The disturbances become dominated by the second mode after synchronization between mode I and the second mode. They pointed out that entropy layer and nose bluntness effects are two major factors that affect the receptivity over blunt cones. The receptivity path they found is different from the one of freestream fast acoustic waves over a flat plate in Ma and Zhong [8]. Such comparison shows that the receptivity mechanism over different geometries can be significantly different.

Fedorov et al. [19,20] performed a numerical simulation of temporally sinusoidal temperature spots over a flat plate in a Mach 6 flow. They computed a case with the temperature spots initially imposed at a short distance above the boundary layer in the flowfield behind the oblique shock and another case with the temperature spots initially imposed in front of the shock at a short distance above the level of the plate. In the first case, the temperature spots generated mode F near the edge of the boundary layer. Then, the second mode was excited by the synchronization between mode S and mode F via the intermodal exchange mechanism that is discussed by Fedorov and Khokhlov [21]. The new terminology of discrete mode S and mode F is discussed in Fedorov and Tumin [22]. The latter case involved the shock/spot interaction. It generated acoustic waves that penetrated into the boundary layer and excited mode S. The instability amplitudes of the latter case are an order of magnitude higher than those in the first case.

Heitmann and Radespiel [23] performed numerical simulations of flow perturbed by a laser spot that was initially imposed above the boundary layer and behind the bow shock of a sharp straight cone in a Mach 5.85 freestream. They also performed an experimental study

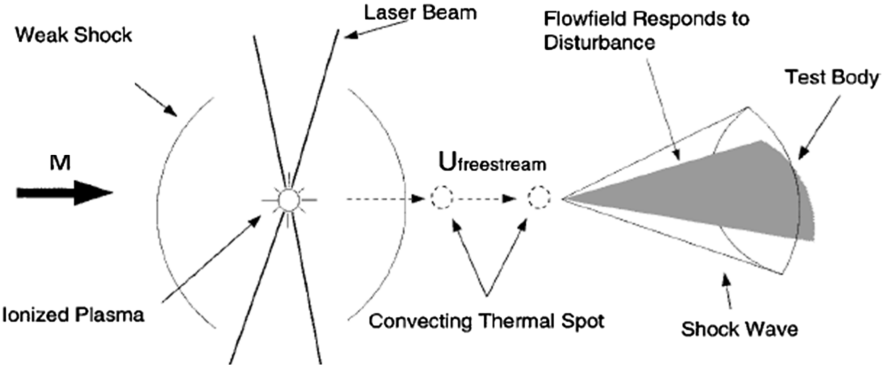

Fig. 1 Schematic of the experimental laser spot and cone scenario in Schmisseur et al. [12].

for the same laser spot setup and cone in a Mach 6 freestream [24]. Their laser spot was acoustic-wave-dominant rather than entropy-wave-dominant. The results of their experiment compared reasonably well with their simulation, which showed that imposing the laser spot could lead to the second-mode instability. Their focus is on the subsequent disturbance growth and wave interactions downstream rather than the receptivity mechanism.

From the previous studies, we found that it is necessary to conduct a new simulation study and an initial LST-based analysis of the receptivity mechanisms to freestream entropy perturbations with a wide continuous frequency spectrum for a hypersonic flow over a blunt cone with the effects of the entropy layer and bow shock. This is a much more complex flowfield compared to the past studies for receptivity to freestream acoustic waves at a few discrete frequencies [1,5–7] or for a simple flat plate without the bow-shock effects [9,20]. The previous studies conducted with freestream entropy waves over a cone were mainly preliminary experimental studies and a simulation study with an emphasis on wave interactions at the later part of the flowfield, not the initial receptivity process [12,23,24]. Therefore, the receptivity mechanisms over a blunt cone for freestream entropy spot with a wide frequency range have not been studied before, and the conclusions of previous studies cannot be extrapolated to the new study without detailed analyses.

In order to carry out the receptivity study of freestream entropy perturbations with a wide continuous frequency spectrum for a hypersonic flow over a blunt cone, the main objectives of this paper are 1) to systematically study the behavior of the boundary-layer disturbances throughout the receptivity process over a wide frequency spectrum, 2) to investigate the linear boundary-layer receptivity mechanism to freestream entropy spot (hotspot) perturbations, and 3) to build a receptivity database for reconstructing the boundary-layer disturbances in a linear receptivity regime under general freestream entropy forcing. Such database provides the initial condition for the study of nonlinear boundary-layer disturbance development [25].

The numerical study of this paper is motivated by the ongoing Mach 6 compression-cone receptivity experiments at Purdue University [18,26]. Thus, the compression cone designed by Wheaton et al. [16] (see Fig. 2) is selected. It is a circular blunt cone with a circular-flared geometry along its body. The flow conditions that were used in our study are also identical to the Mach 6 tunnel conditions in Wheaton et al. [16]. The compression-cone geometry causes earlier transition when compared to a corresponding straight cone owing to the adverse pressure gradient that occurs along the flared geometry of the cone [1,16]. This geometry also makes the boundary-layer thickness approximately constant in the downstream direction. As a result, the second-mode frequencies do not alter much along the cone [16].

The numerical study in this paper consists of three parts: 1) the steady base flow simulation and the LST analysis, 2) the unsteady flow simulation with the freestream hotspot perturbations imposed, and 3) the investigation on the receptivity mechanism and the second-mode development by comparing the simulated results with the LST analysis.

II. Governing Equations and Numerical Methods

The current simulation of the axisymmetric hypersonic perfect-gas flow around a compression cone is two-dimensional (i.e., it does not depend on the circumferential coordinate). However, the code that is written to perform the simulation is capable of computing a three-dimensional flow. Thus, the governing equations in the code are the three-dimensional Navier–Stokes equations in conservative-law form and in Cartesian coordinates:

$$\frac{\partial U^*}{\partial t^*} + \frac{\partial F_j^*}{\partial x_j^*} + \frac{\partial F_{vj}^*}{\partial x_j^*} = 0, \qquad (j = 1, 2, 3) \tag{1}$$

The tensor notation (x_1^*, x_2^*, x_3^*) represents the Cartesian coordinates (x^*, y^*, z^*). The vector $\boldsymbol{U}^*$ contains five conservative flow variables:

$$\boldsymbol{U}^* = [\rho^* \quad \rho^* u_1^* \quad \rho^* u_2^* \quad \rho^* u_3^* \quad e^*]^T \tag{2}$$

where F_j^* and F_{vj}^* are defined as

$$F_j^* = \begin{bmatrix} \rho^* u_j^* \\ \rho^* u_1^* u_j^* + p^* \delta_{1j} \\ \rho^* u_2^* u_j^* + p^* \delta_{2j} \\ \rho^* u_3^* u_j^* + p^* \delta_{3j} \\ (e^* + p^*) u_j^* \end{bmatrix} \tag{3}$$

$$F_{vj}^* = \begin{bmatrix} 0 \\ -\tau_{1j}^* \\ -\tau_{2j}^* \\ -\tau_{3j}^* \\ -\tau_{jk}^* u_k^* - q_j^* \end{bmatrix}, \qquad (k = 1, 2, 3) \tag{4}$$

The equation of state and transport equations are

$$p^* = \rho^* R^* T^* \tag{5}$$

$$e^* = \rho^* \left(c_v^* T^* + \frac{1}{2} u_k^* u_k^* \right) \tag{6}$$

$$\tau_{ij}^* = \mu^* \left(\frac{\partial u_i^*}{\partial x_j^*} + \frac{\partial u_j^*}{\partial x_i^*} \right) - \lambda^* \frac{\partial u_k^*}{\partial x_k^*} \delta_{ij}, \qquad \lambda^* = \frac{2}{3} \mu^* \tag{7}$$

$$q_j^* = -\kappa^* \frac{\partial T^*}{\partial x_j^*} \tag{8}$$

where c_v^* is constant with a given γ, and κ^* can be determined with a constant Prandtl number. The viscosity coefficient is defined by Sutherland's law:

$$\mu^* = \mu_r^* \left(\frac{T^*}{T_r^*} \right)^{\frac{3}{2}} \left(\frac{T_r^* + T_s^*}{T^* + T_s^*} \right) \tag{9}$$

A high-order shock-fitting method can accurately resolve the location and velocity of the bow shock, which is necessary to obtain high-ordered accuracy of the flow solutions for receptivity and stability analyses [27]. Thus, in this paper, the high-order shock-fitting method is used to compute both steady and unsteady hypersonic viscous flow over a blunt cone. To apply the shock-fitting method, the Navier–Stokes equations in Cartesian coordinates

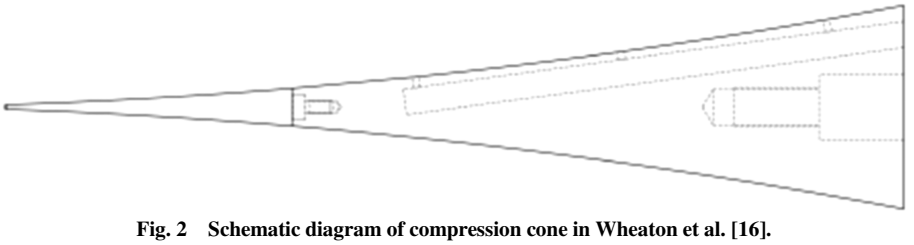

Fig. 2 Schematic diagram of compression cone in Wheaton et al. [16].

(x^*, y^*, z^*, t^*) are transformed into body-fitted curvilinear computational domain coordinates (ξ, η, ζ, τ). The body-fitted curvilinear computational domain is bounded between the bow shock and the wall of the blunt cone. Figure 3 demonstrates a partial view of the computational domain.

The spatial discretization of the inviscid flux derivatives in the streamwise and the wall-normal directions are done using a fifth-order finite-difference upwind scheme with a local Lax–Friedrichs flux-splitting formulation. A sixth-order central finite-difference scheme is used for the spatial derivatives of the viscous flux in the streamwise and the wall-normal directions. For spatial derivatives of both the inviscid and viscous fluxes in the periodic azimuthal direction, Fourier collocation is used. Runge–Kutta is used for time marching.

In Fig. 3, the computational domain has four boundaries. The boundary at the shock is computed using Rankine–Hugoniot normal-shock relations. The surface of the wall is assumed to be no-slip and isothermal. The pressure at the wall is computed from the flowfield by using a high-order polynomial extrapolation. The boundary at the stagnation line is a singularity in the current computational domain; thus, it is extrapolated by a high-order polynomial. The exit boundary is also computed by a high-order polynomial extrapolation owing to supersonic flow at the exit. The details of the shock-fitting formulations and the high-order finite-difference schemes are explained in Zhong [27].

Zhong [27] presented a high-order shock-fitting method for the simulation of the hypersonic flowfield bounded by the shock and the wall of a blunt body. The numerical experiments for the shock-fitting method were to compute the steady flow over a two-dimensional cylinder and the unsteady periodic flow over a parabolic leading edge at zero angle of attack with two-dimensional and oblique three-dimensional freestream acoustic waves. The results of the flow over the cylinder were validated with those of the shock-fitting spectral method and the experiment. The results of the flow over the parabolic leading edge are validated with the LST and the linear-shock theory.

III. Model for Freestream Entropy Spot Perturbations

Aiming to incorporate a hotspot into the simulation, the spot needs to be represented by a modeling equation. The previous freestream benchmark tests of the laser spot shows that it has an approximately Gaussian temperature or density profile with a weak shock surrounding it [12–15]. Because the weak shock dissipates very rapidly while the entropy core remains mostly constant in the freestream, the influence of the weak shock can be minimized by calibrating the initial distance between the laser spot and the bow shock. Therefore, a hotspot model of Gaussian entropy perturbations is used in the current numerical study. This model contains the main features of a hotspot.

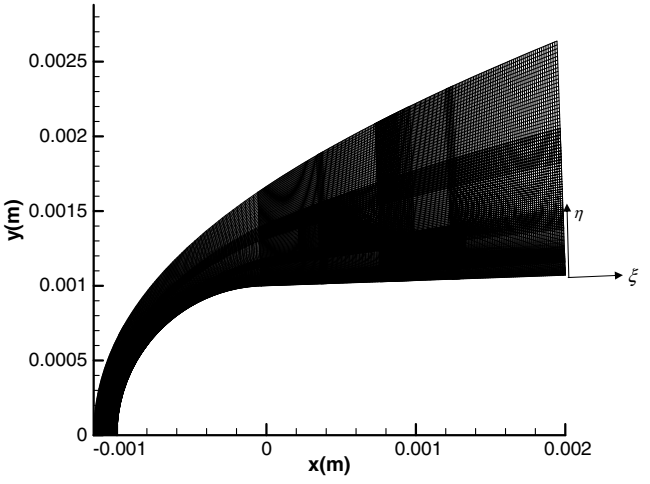

Fig. 3 Partial view of grid configuration in zones 1, 2, and 3 near the nose region.

In this paper, the freestream hotspot is modeled by Gaussian entropy perturbations. Specifically, the temperature profile in the freestream is

$$T^*(x^*, y^*, z^*, t^*) = \Delta T^*_{\max} \exp\left(-\frac{R_c^{*2}}{2\sigma^2}\right) + T^*_\infty \tag{10}$$

where σ is a Gaussian shaping factor, $\Delta T^*_{\max}$ is the maximum freestream temperature perturbation amplitude, and R_c^* is the radial distance from the center of entropy spot to any point (x^*, y^*, z^*) in space, i.e.,

$$R_c^* = \sqrt{(x^* - x^*_{\text{spot}})^2 + (y^* - y^*_{\text{spot}})^2 + (z^* - z^*_{\text{spot}})^2} \tag{11}$$

In Eq. (11), $(x^*_{\text{spot}}, y^*_{\text{spot}}, z^*_{\text{spot}})$ is the instantaneous coordinate of the center of the entropy spot:

$$\begin{cases} x^*_{\text{spot}} = x^*_0 + u^*_\infty t^* \\ y^*_{\text{spot}} = y^*_0 = 0 \\ z^*_{\text{spot}} = z^*_0 = 0 \end{cases} \tag{12}$$

where u^*_∞ is the freestream velocity. In Eq. (12), (x^*_0, y^*_0, z^*_0) is the initial coordinate of the center of entropy spot at $t^* = 0$. Here, y^*_{spot} and z^*_{spot} are zero because the hotspot in the freestream is located at the x axis, or the centerline of the cone.

From the ideal gas law, the perturbed freestream density is

$$\rho^*(x^*, y^*, z^*, t^*) = \frac{p^*_\infty}{R^* T^*} \tag{13}$$

where P^*_∞ is a constant because there are no acoustic perturbations in the freestream.

IV. Spectral Analysis of Boundary-Layer Instability

In the simulation, the perturbations induced by the hotspot traveling along the cone surface contain a wide range of frequencies. To study the instability of the wave components of each individual frequency, a temporal Fourier spectrum analysis is performed on the perturbation flow variables.

An arbitrary flow-variable time function $h(t)$ is represented in terms of the discrete spectral components as

$$h(t_k) \equiv h_k \approx \sum_{n=0}^{N-1} H(F_n) e^{-2\pi i F_n t_k} \tag{14}$$

where $H(F_n)$ is the spectral value at the nth discretized frequency F_n, and N is the total number of Fourier collocation points that are used to discretize the time function $h(t)$. The discretized time function is h_k, which is defined as the value of $h(t)$ at $t = t_k$.

In this paper, $h(t)$ is the time history of local boundary-layer perturbations, and $H(F_n)$ is the spectral value of the boundary-layer perturbations in the frequency domain. $H(F_n)$ is a complex value, and $|H(F_n)|$ is the local perturbation amplitude.

After obtaining the frequency spectra of the boundary-layer perturbations from the unsteady simulation, the local spatial growth rates, local wave numbers, and the wall-normal boundary-layer mode shapes are then compared with LST for the receptivity study. Local growth rates are determined by [2]

$$-\alpha_i = \frac{1}{|H(F_n)|} \frac{\mathrm{d}|H(F_n)|}{\mathrm{d}s} \tag{15}$$

Local wave numbers are determined by [2]

$$\alpha_r = \frac{\mathrm{d}\varphi_n}{\mathrm{d}s} \tag{16}$$

Table 1 Freestream conditions

Parameter	Value
M_∞	6.0
ρ^*_∞	0.0403 kg/m^3
T^*_∞	52.8 K
T^*_o	433.0 K
T^*_{wall}	300.0 K
γ	1.4
Pr	0.72
R^*	287.04 N · m/kg · K(air)
μ^*_r	1.7894×10^{-5} kg/m · s(sea level)
T^*_r	288 K (sea level)
T^*_s	110.3 K
Re^*_∞	1.026×10^7 m^{-1}

where φ_n is the phase angle of $H(F_n)$ at the nth discretized frequency. The wall-normal mode shape is the spatial distribution of the local perturbation amplitude $|H(F_n)|$, along the normal to the cone surface.

V. Freestream Flow Conditions and Compression-Cone Geometries

The freestream conditions are based on those of the Mach 6 quiet tunnel (BAM6QT) at Purdue University [16]. The cone that is placed in freestream has zero angle of attack. The flow around the cone is assumed to be axisymmetric. The wall of the cone is smooth, rigid, and isothermal. The details of the freestream conditions are summarized in Table 1.

The geometry of the blunt compression cone is the same as that used in the experimental studies by Wheaton et al. [16]. It consists of two parts: a spherical nose section followed by a flared section. The spherical nose of the cone is blunt with a small radius of 1 mm. The starting point of the flared surface is tangent to the spherical nose surface with an initial angle of 2 deg. The flared geometry has a circular arc of 3.0 m in radius. The total length of the cone, which measures from the tip of the spherical nose to the base of the cone along the centerline, is 0.45 m. The schematic of the blunt compression cone is illustrated in Fig. 2.

VI. Simulation Results

Because of the limited computer power for computing a huge amount of grid points at once, the simulation is divided into 21 zones. Zone 1 is the computation domain in the stagnation region over the hemispherical cone nose. Zone 2 to zone 21 is the computation domain in the compression region over the cone. For zone 1 to 12, the total grid resolution is 2280×120. For zone 13 to 21, the total grid resolution is 2160×240. The periodic azimuthal direction has four points to resolve the axisymmetric flow in the spectral method. Figure 3 shows the partial view of the computational grid around the cone. The reflection, which is created during the exiting of the disturbances at the downstream boundary of each zone, is minimal due to overlap regions. During the computation, the profiles of the disturbances at different frequencies nearby the exit of each zone are monitored to make sure there is enough overlap points in the streamwise direction for the inlet of the next zone to skip the reflection affected area. The computation of each zone lasts until the disturbances fully exit the zone. At the end of the computation, the overall relative amplitude of the perturbations in each zone is $\mathcal{O}(10^{-9})$. The maximum time-step size of recording the unsteady inlet boundary conditions is 1.12×10^{-7} s, which is sufficient to resolve the second-mode instability at the high end of the studied frequency range. It is worth to notice that the current zonal method used in our simulations is fundamentally the same as the flow with periodic flows published [5,9,27].

The grid-convergence study of steady base flow is carried out with two grids in Sec. IV of Lei and Zhong [28]. The freestream Mach number used in their grid-convergence study is 5.5, and their freestream unit Reynolds number is 1.9×10^7 m^{-1}, which is higher than the current case. The cone used in their study is a straight blunt cone with a nose radius of 4 mm, and the half-angle of the cone is 8 deg. Based on the fact that a case with a higher freestream unit Reynolds number requires a higher computational resolution, the resolution independence study not only shows that both sets of 120 and 240 grid points in wall-normal direction are sufficient for their simulation but also for the one in this paper. The grid-convergence study of the current unsteady flow is presented in Sec. VI.D.

A. Steady Base Flow Solutions

The first part of the study in this paper is to simulate the steady base flow over the compression cone. The Mach-number contours in Fig. 4 and the Mach-number profiles at various locations in Fig. 5 show that the Mach number near the wall increases drastically over a short distance behind the nose region, and it gradually decreases downstream along the cone where the adverse pressure gradient occurs on the concave surface of flaring of the cone. Eventually, a region of relatively low Mach number appears above the wall near the bottom of the cone. The thickness of the Mach boundary layer is consistently about 0.001 m in Figs. 5b–5d. The constant boundary-layer thickness prevents the shift of the unstable frequency, which is discussed in Sec. VI.D. There is a dent near the top of the profile in Fig. 5d. It is the Mach waves developed under the compression effects of the concave cone surface. At further downstream locations beyond the current computation domain, it could eventually form a shock outside the boundary layer. Such Mach waves are seen in the steady base flow over a flared cone in Mach 6 freestream by Zhong [1] as well.

Wheaton et al. [16] computed their steady base flow by using STABL. Their flow conditions and cone geometry are the same as those used in the current study. The same physical phenomena observed in Fig. 4 are seen in their steady base flow. To compare the current steady base flow with Wheaton et al. [16], the current shock shape is overlaid to the one of Wheaton et al. [16] in Fig. 6. In this figure, both shock shapes compare reasonably well with each other. This observation shows that the computation that is done by the current shock-fitting code is consistent with other methods.

B. Linear-Stability Theory

LST is based on a linear disturbance growth governed by the linearized Navier–Stokes equations [2]. The LST code that is used in the current study is based on Malik's multidomain spectral collocation method [29] and was implemented in Lei and Zhong [28].

The disturbances in the current simulation are two-dimensional and are not dependent on the azimuthal coordinate. Thus, in LST, the normal mode of disturbances has the form

$$q' = \hat{q}(y_n)e^{i(-\omega t+\alpha s)} \tag{17}$$

where q' is the nondimensional disturbances of an arbitrary flow variable normalized by its corresponding freestream quantity. $\hat{q}$ is the complex amplitude of the disturbances.

In spatial stability theory, ω is a real number. The streamwise wave number α has a real part α_r and an imaginary part α_i. α_r is the spatial

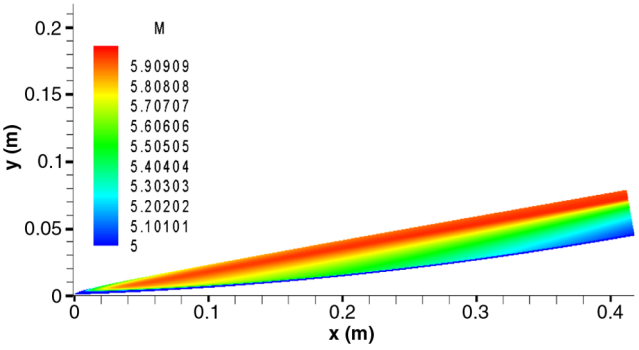

Fig. 4 Mach-number contours of the steady base flow.

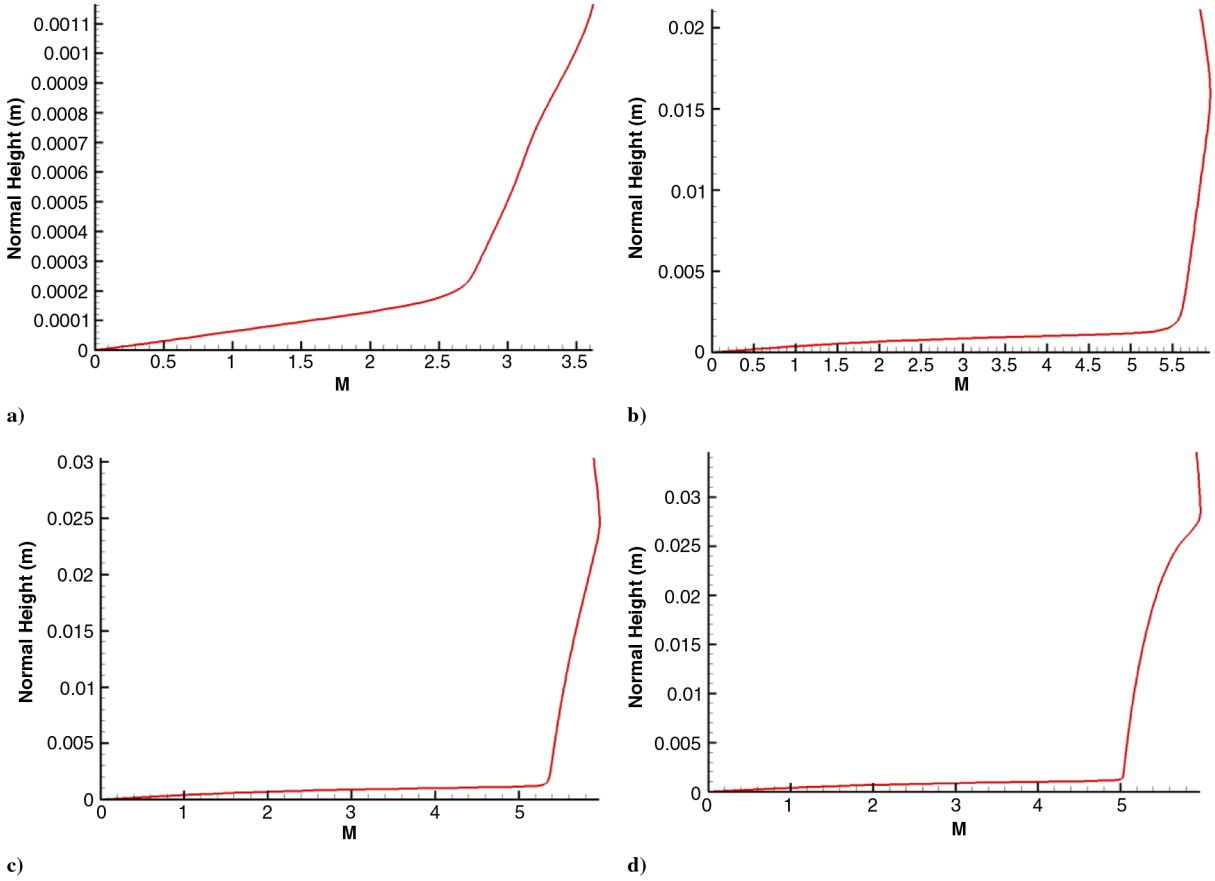

Fig. 5 Mach-number profiles of steady base flow at four locations along the cone surface: a) $x^* = 0.001$ m, b) $x^* = 0.138$ m, c) $x^* = 0.258$ m, and d) $x^* = 0.418$ m.

wave number, and $-\alpha_i$ is the spatial growth rate of a disturbance mode. In LST studies, a local Reynolds number based on the length scale of the boundary-layer thickness can be used, where

$$R = \frac{\rho_\infty^* u_\infty^* L^*}{\mu_\infty^*} \tag{18}$$

The length scale of the boundary-layer thickness is

$$L^* = \sqrt{\frac{\mu_\infty^* s^*}{\rho_\infty^* u_\infty^*}} \tag{19}$$

Thus, a relation between the freestream unit Reynolds number, and R is

$$R = \sqrt{s^*(Re_\infty^*)} \tag{20}$$

The disturbance frequency is characterized by a dimensionless frequency:

$$F = \frac{\omega^* \mu_\infty^*}{\rho_\infty^* u_\infty^{*2}} \tag{21}$$

The dimensionless circular frequency and the dimensionless complex wave number are defined as

$$\omega = \frac{\omega^* L^*}{u_\infty^*} \tag{22}$$

$$\alpha = \alpha^* L^* \tag{23}$$

The relation between dimensionless circular frequency and dimensionless frequency becomes

$$\omega = RF \tag{24}$$

The dimensionless phase speed of the disturbances in the streamwise direction is related to the wave number by

$$a = \frac{\omega}{\alpha_r} \tag{25}$$

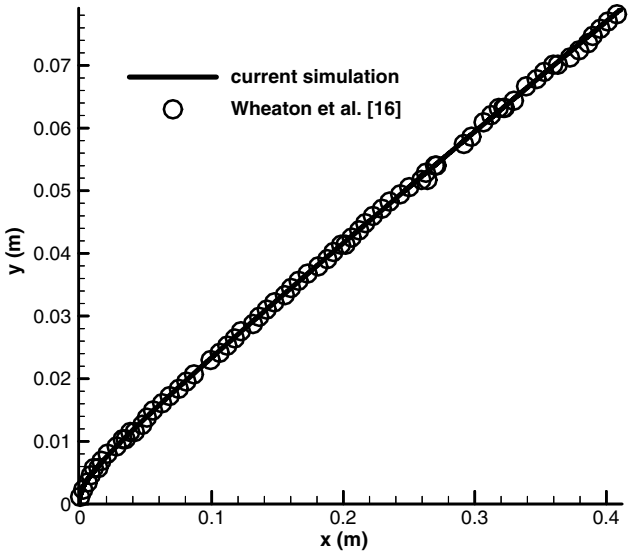

Fig. 6 Comparison of shock fronts of steady base flow between the current simulation and the one of Wheaton et al. [16].

The dimensionless phase speed is normalized by the freestream velocity.

For unstable waves, the growth of amplitudes can be measured by an N-factor. An N-factor is the exponential power index of the amplification rate A/A_0, which is the ratio of an amplified disturbance amplitude to its initial unamplified disturbance amplitude, namely

$$e^N = \frac{A}{A_0} = \exp \int_{s_0^*}^{s^*} \frac{1}{A}\frac{\mathrm{d}A}{\mathrm{d}s}\,\mathrm{d}s^* \tag{26}$$

Hence, an N-factor is the integration of the spatial growth rate from the neutrally stable location s_0^* to an arbitrary location s^*:

$$N = \int_{s_0^*}^{s^*} -\alpha_i^*\,\mathrm{d}s^* \tag{27}$$

From Eq. (27), an N-factor represents the accumulative relative change from the neutrally stable location to an arbitrary location downstream. In the e^N method for transition prediction, the location of laminar–turbulent transition is empirically related to a critical value of the N-factor. In a low-noise wind tunnel, the typical critical N-factor for sharp cones is 8 to 11 [16]. Thus, at any downstream location where the N-factors are larger than or equal to that of the critical range, transition is expected to occur.

For the flow over the compression cone, LST analysis is performed, and the current results are compared with those by Wheaton et al. [16] for validation of both the steady base flow and the LST code. They performed LST and PSE analyses on their steady base flow over the same cone [16]. Five frequencies were used in their LST analysis: 257.498, 271.797, 278.996, 292.494, and 297.494 kHz. Nearly the same set of five frequencies is used in the current LST calculations. Comparisons of our LST results on the N-factors and growth rates of the second mode with LST N-factors and PSE growth rates of Wheaton et al. [16] are shown in Figs. 7 and 8, respectively. The current LST calculation shows that the N-factor reaches 13 and the growth rate reaches 58 m^{-1} at $x^* = 0.42$ m. It is shown in both figures that the results compare well for the highest four frequencies, whereas the differences are larger for the lowest frequency. In addition, both instability onset locations agree well. The magnitudes of the current N-factors and growth rates appear lower than those of Wheaton et al. [16]. This could possibly be caused by the difference in the numerical method that is used to compute the steady base flow. In addition, the LST and PSE code that is used by Wheaton et al. [16] is different from the one used in the current study. The streamwise curvature effect is not considered in the current LST model. Because the detailed LST and PSE models are not provided in their paper, the authors are unable to investigate further.

It is noticed that, even though the neutral stability curve is not directly linked to receptivity because forcing waves are not included in the LST analysis, the neutral stability curve is still relevant to receptivity because the forcing leads to instability governed by the curve. For this reason, the neutral stability curve is shown in Fig. 9 to demonstrate the general stability properties of this flow. The critical location is $s^* = 0.109$ m at a frequency of 298 kHz. At a location where $s^* < 0.109$ m, the boundary-layer waves are stable. The wave components of lower frequencies ($F^* < 298$ kHz) become unstable much earlier than those of higher frequencies ($F^* > 298$ kHz). Such observation implies that the instability tends to occur at lower frequencies. In the other words, the higher-frequency components are more stable.

C. Unsteady Flow Solutions with Hotspot Perturbations in the Freestream

In the current study, we consider the axisymmetric flowfield with the axisymmetric freestream hotspot that is initially aligned with the centerline of the cone. The freestream hotspot has a radius of approximately 0.003 m. The radial Gaussian temperature profile of the hotspot in the freestream is shown in Fig. 10. At the center of the hotspot, the temperature is maximal, and the radial coordinate is zero. The hotspot is initially placed at a location not far upstream from the bow shock along the centerline of cone. The hotspot core radius is controlled by a dimensionless Gaussian factor σ. In the current study, the dimensionless Gaussian factor is 0.001. The shape parameters of the freestream hotspot perturbations are based on the laser spot experiments of Salyer et al. [14,15].

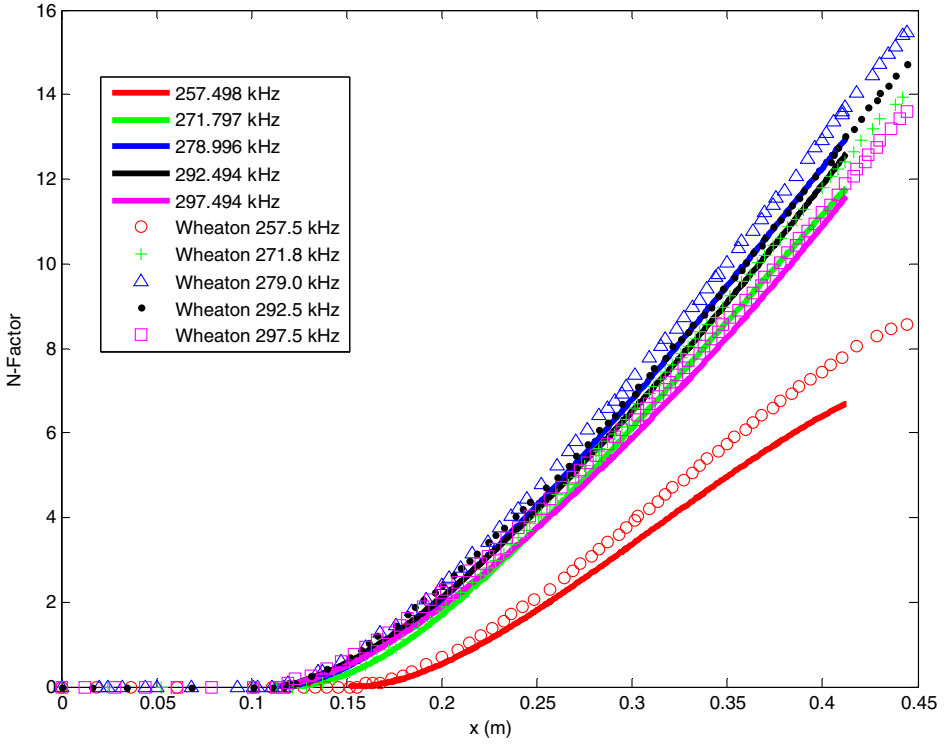

Fig. 7 Comparison of the second-mode N-factors from the current LST analysis with those of Wheaton et al. [16].

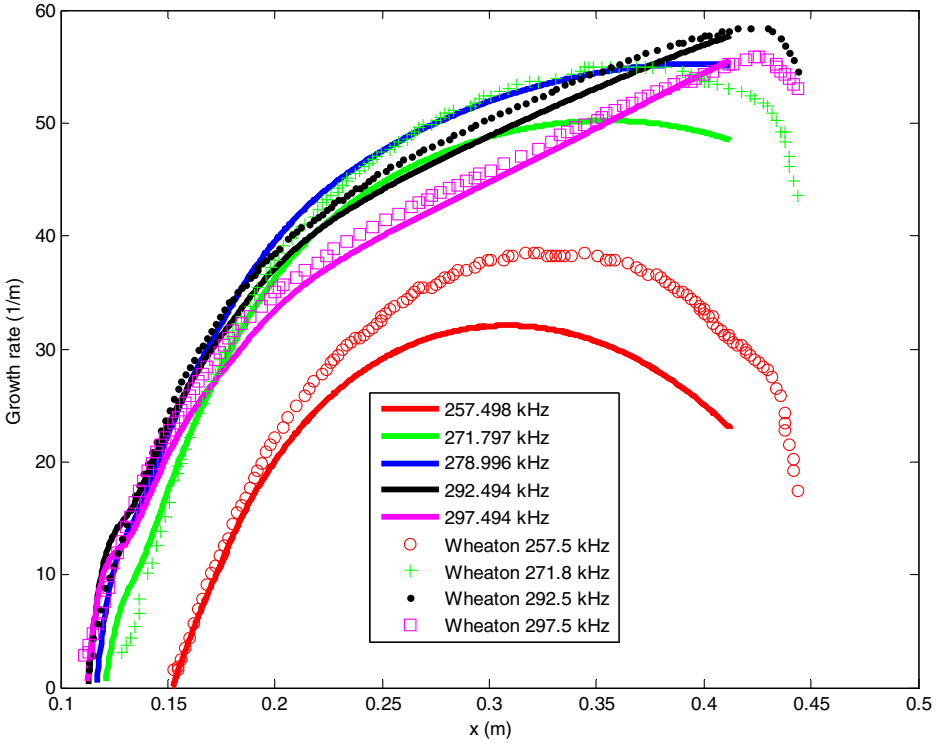

Fig. 8 Comparison of the second-mode growth rates from the current LST analysis with those of Wheaton et al. [16].

The receptivity process in the current study is in the linear regime; thus, the hotspot with very weak amplitude is imposed in the freestream. Previously, Ma and Zhong [9] and Zhong and Ma [5] chose their freestream relative perturbation amplitudes to be $\mathcal{O}(10^{-4})$ to keep the development of boundary-layer disturbances within the linear regime. Therefore, the freestream maximum relative amplitude of temperature perturbations at the center of hotspot, ε, is chosen to be

$$\varepsilon = \frac{\Delta T_{\max}}{T_\infty} = 10^{-4} \tag{28}$$

Having obtained a steady base flow solution, the unsteady numerical simulation is performed by imposing hotspot perturbations into the freestream in front of the bow shock. The Gaussian formulations given by Eqs. (10–13) are used to analytically model a three-dimensional hotspot that is convecting the freestream. Moreover, the freestream hotspot is imposed onto the computational domain as an unsteady shock boundary condition.

The flow-variable perturbations shown in Figs. 11–16 are normalized by the corresponding freestream flow variables (i.e., P'^*/P^*_∞ and S'^*/S^*_∞). The structures of hotspot perturbations in the nose region over the cone are demonstrated in Figs. 11 and 12. This is the region where the hotspot first enters the shock layer. The magnitude of pressure perturbations in Fig. 11 reaches a local maximum at the stagnation point. The entropy perturbations in Fig. 12 have a maximum absolute magnitude at the stagnation line next to the bow shock. In addition, the small length scale of the entropy waves next to the wall near the stagnation point is a consequence of the fact that entropy waves move at the local flow velocity without reflection at the wall. In contrast with the entropy waves, acoustic waves propagate and are reflected at the wall toward the bow shock. As a result, Fig. 11 shows the pressure perturbations that do not have the small length scale wave next to the wall near the stagnation point. The hotspot enters the shock layer from the freestream, and it travels downstream with the flow. Eventually it

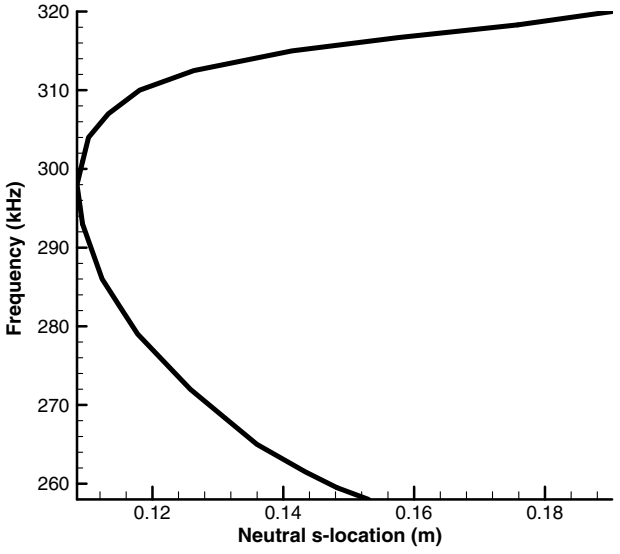

Fig. 9 Neutral stability curve of the second mode.

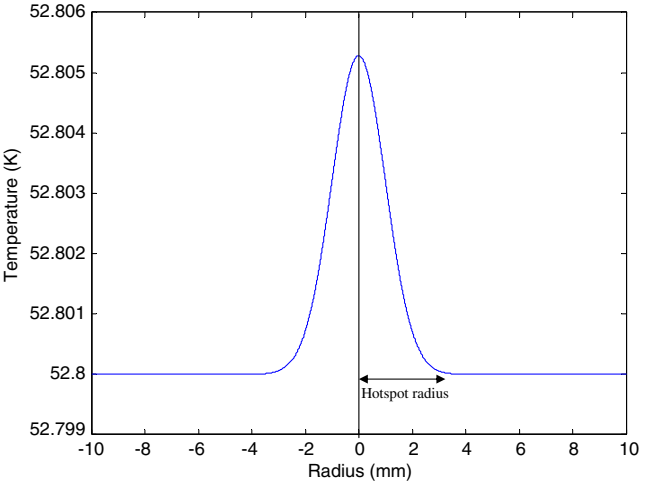

Fig. 10 Gaussian distribution of perturbed temperature in radial direction.

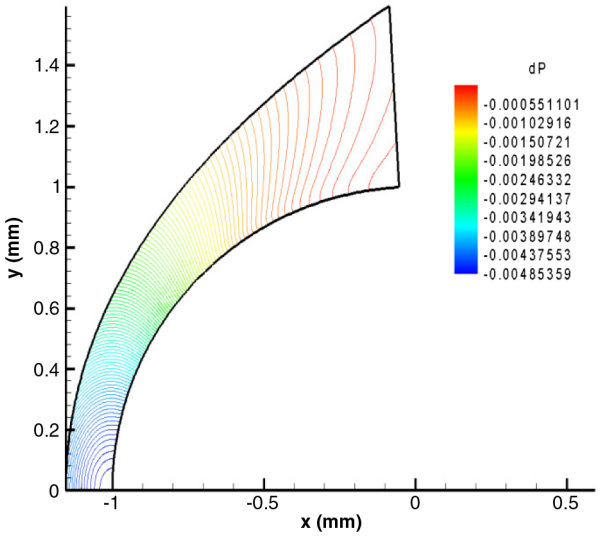

Fig. 11 Contours of hotspot pressure perturbations behind the shock in nose region over the compression cone.

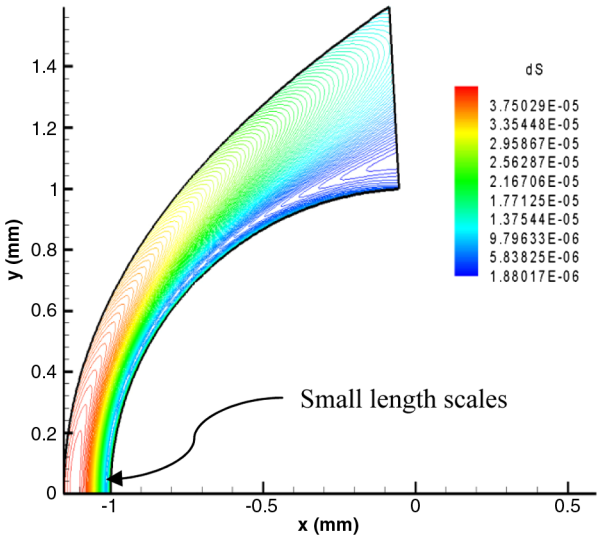

Fig. 12 Contours of hotspot entropy perturbations behind the shock in nose region over the compression cone.

passes through the rightmost exit boundary of the nose region and moves into the next computation zone.

As the hotspot travels further into the middle region of the cone, the size of the hotspot is much wider and longer when compared to the hotspot in the upstream region. The structures of hotspot perturbations in the middle region over the cone are demonstrated in Figs. 13 and 14. Because the size of a single computation zone is not large enough to demonstrate the entire hotspot in a single snapshot, several snapshots are used to demonstrate the parts of the hotspot passing by a zone. The main body of the pressure perturbations has two parts: the front part and the rear part. The front part contains fast acoustic waves that travel ahead in the hotspot main body. The rear part that contains slow acoustic waves travels behind the front part in the main body. The entropy perturbations are also shown in two parts: the main body and the first tail (there will be another tail, namely the second tail, which appears behind the first tail in the downstream region). The first tail travels behind the main body, and it is oscillatory.

As the hotspot reaches the downstream region of the cone, the unstable waves appear in the tail, which travels slower than the main body of the hotspot. The flow structures of hotspot perturbations in the downstream region over the cone are demonstrated in Figs. 15 and 16. The pressure perturbations are shown in three sections in Fig. 15. In this region, an oscillatory tail appears behind the main body of pressure perturbations. The main body, which consists of a front and a rear part, becomes subdominant in wave amplitudes while the perturbations in the tail exceed those of the main body in this region.

The entropy perturbations are shown in Fig. 16. The first tail in entropy perturbations is oscillatory. The entropy perturbations in the main body of the hotspot are weaker than those in the middle region. The second tail appears behind the first tail. Meanwhile, the first tail is weaker than the second tail. The waves in the second tail have the highest amplitude in the entire wave packet. The second tail of entropy perturbations is "rope" structured waves located at the edge of the boundary layer. The wavelength of these rope waves is approximately twice of the boundary-layer thickness. These are the typical features of the second-mode-dominated waves [30].

D. Boundary-Layer Receptivity Analysis

The numerical solution for the time history of the wall-pressure perturbations is recorded at various spatial locations along the cone surface. Figures 17 and 18 show the time-history traces of wall-pressure perturbations, where the pressure perturbations are normalized with respect to the freestream pressure.

Figure 17 shows the wall-pressure perturbations traveling through the upstream part of the cone. In the upstream part of the cone, the perturbation time-history profiles start with a relatively monotonic

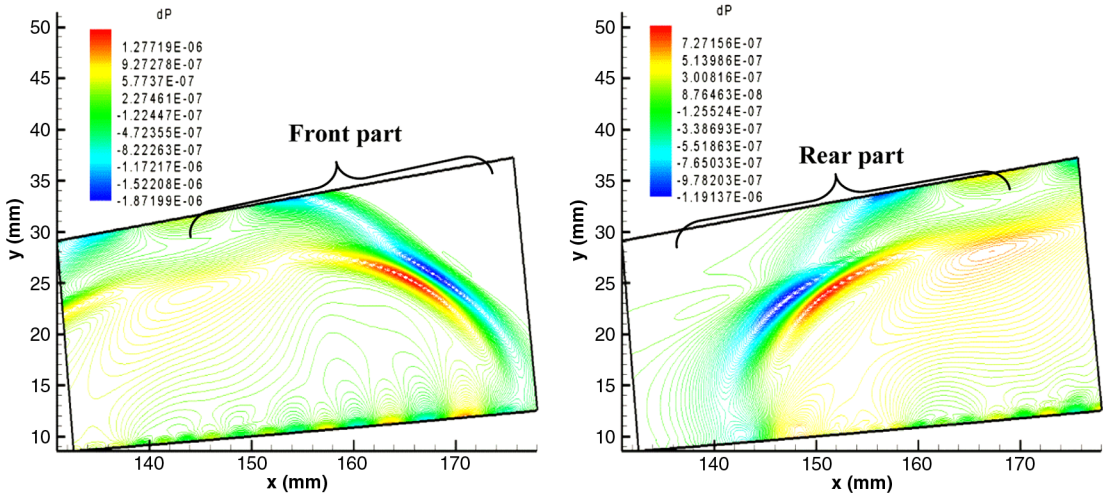

a) b)

Fig. 13 Contours of hotspot pressure perturbations in middle region over the compression cone: a) front part, and b) rear part.

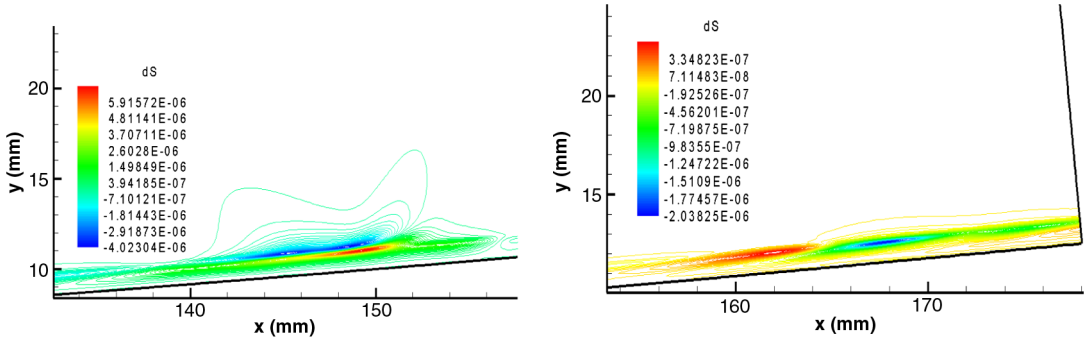

a) b)

Fig. 14 Contours of hotspot entropy perturbations in middle region over the compression cone: a) main body, and b) first tail.

shape. They gradually decay while traveling downstream and split into a multipeak shape. In the range from $x^* = 0.0337$ to 0.0925 m, the profile has the frequency around 160 kHz, which falls in the frequency range of the possible stable first mode (120 to 240 kHz) that is discussed in latter part of this section. The perturbations are indeed likely to be stable first-mode-predominant. However, there are initial transients and other wave modes existing in the perturbations as well. Thus, further investigation is needed to confirm this point. Because the stable first mode is not as important as the unstable second mode in this flow, we did not investigate it in detail. Instead, we mainly focus on the unstable second mode.

Figure 18 shows the wall-pressure perturbations in the downstream part of the cone. In this region, multipeak-shaped perturbations begin to split into two parts in time: one with a more oscillatory followed by another with a smoother profile. These waves are associated with the main body (the front part and the rear part) of the pressure perturbations in Figs. 13 and 15. The more oscillatory part has the frequency about 160 kHz. The waves are indeed likely to be stable first-mode-predominant. As the hotspot induced perturbations travel further downstream, the perturbation amplitudes decay. Starting at $x^* = 0.25$ m, or 56% of the total cone length, a new perturbation waveform appears. The amplitudes of this new waveform grow rapidly. The amplitudes of this new waveform soon surpass those of the original decaying ones and become the dominant instability in the boundary layer. This new waveform is most likely to be related to the second mode. At the same locations of the wave growth, a

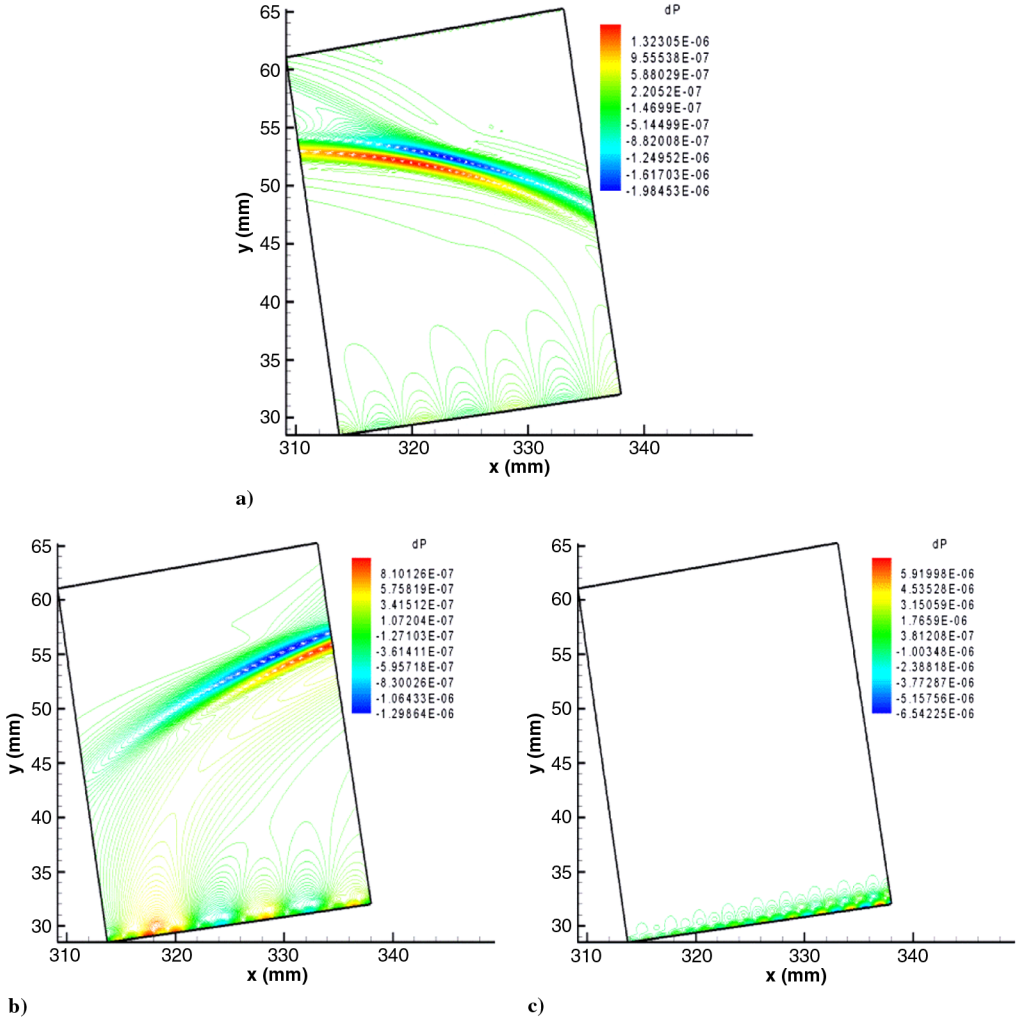

a)

b) c)

Fig. 15 Contours of hotspot pressure perturbations in downstream region over the compression cone: a) front part, b) rear part, and c) tail.

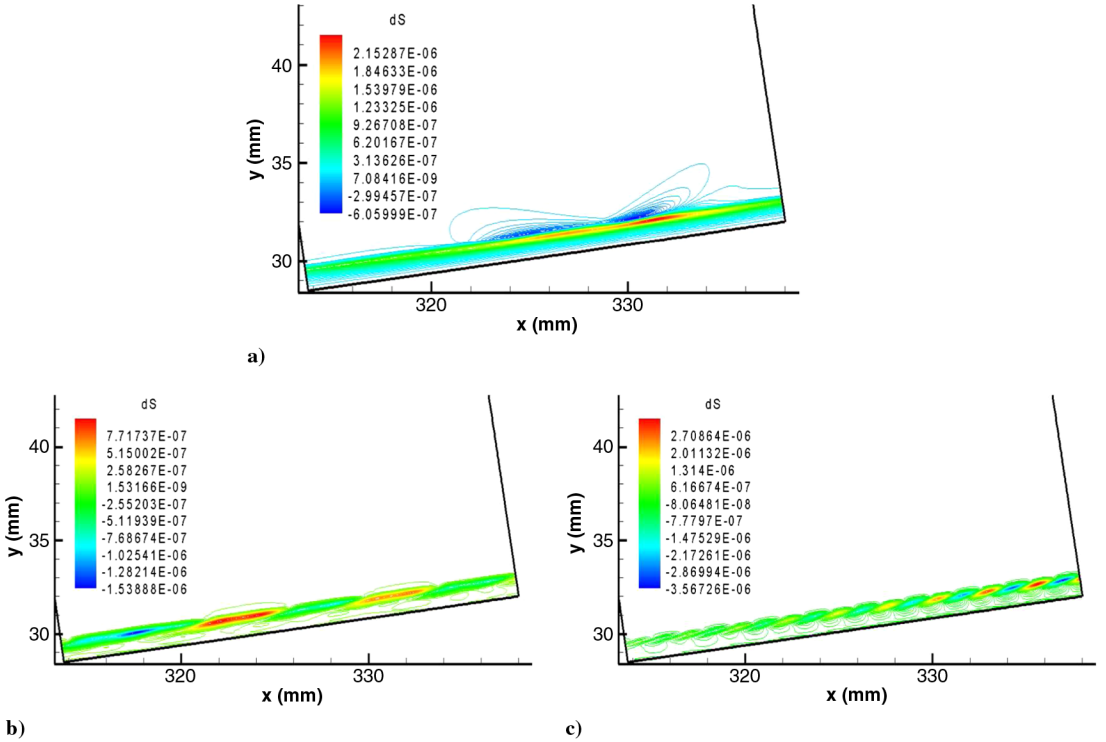

Fig. 16 Contours of hotspot entropy perturbations in downstream region over the compression cone: a) main body, b) first tail, and c) second tail.

less-dominant growing waveform also appears ahead of the most dominant waveform. These two new wave structures can be seen clearly in the profile at $x^* = 0.333$ m in Fig. 18. Specifically, the most dominant one is centered around $t^* = 0.54$ ms, whereas the less-dominant one is located around $t^* = 0.49$ ms. The frequency of the most dominant growing waves is found to be around 291 kHz, and the one of the less-dominant growing waves is 285 kHz. Both waves fall in the frequency range of the second mode. The furthest computed location in current numerical simulation is $x^* = 0.394$ m. The maximum relative magnitude of the second-mode-dominated pressure waves to the local steady base flow pressure reaches $\mathcal{O}(10^{-5})$ at this surface location [31].

To investigate the mechanism of boundary-layer instability induced by the hotspot, Fourier transformation based on the time history of wall-pressure perturbations is carried out at various surface locations. The details are shown in Sec. IV. The simulated perturbations are single impulse, which is temporally "transient" (i.e., they do not continue to repeat in time at a given location). The transient perturbed flow at a location eventually returns back to its steady base flow after the passage of the perturbations. When conducting the Fourier transformation, the time history of single impulse is windowed with no more perturbations existing on both sides. More specifically, the Fourier transformed amplitudes in the current study are independent of the width of the time window as long as the relative amplitudes of the pressure perturbations at both end are $\mathcal{O}(10^{-9})$. In this way, a periodicity of the signal is assumed in the time domain. The maximum recording time-step size of the time histories is 1.12×10^{-7} s, which is sufficient to resolve the second-mode instability at the high end of the studied frequency range. Our Fourier-transformed results are confirmed to be independent of the time step used when we were postprocessing the data from the simulation using the current windowed-Fourier transformation. The validation of the current windowed-Fourier transformation is completed in a comparison between two cases of an unsteady hypersonic flow over a flat plate with a pulse and a single frequency wave, respectively. The case of a single frequency wave is treated by using the traditional Fourier transformation for periodic waves. The results show that the transformed amplitude of both case compares well; therefore, the current windowed-Fourier transformation of a finite-width pulse can adequately represent a wide spectrum of frequency.

Having a sufficient spatial resolution can minimize numerical error, which will eventually be amplified downstream and affect the accuracy of the simulated results significantly. To ensure the sufficiency of the spatial resolution, a grid-convergence study is conducted by comparing the current results with results from a finer grid. For a wall-bounded flow, the boundary layer contains large gradients of flow variables and should be well resolved to attain accurate results. Therefore, a grid-refinement study is only performed in the wall-normal direction. The essential part of the current paper is the results of the unsteady flow simulation with the transient perturbations. Hence, in the grid-convergence study, the frequency spectra of the pressure perturbations at the wall and the growth rates at a downstream location of $s^* = 0.4$ m with two sets of grids; the current grids of 240 points and the finer grids of 480 points in the wall-normal direction are compared. The comparison of frequency spectra of the pressure perturbations at the wall is shown in Fig. 19a. Within the frequency range of the second mode between 260 and 310 kHz, both spectra compare very well. The relative error of the normalized amplitude within the frequency range of the second mode is $\mathcal{O}(10^{-3})$. The comparison of the growth rates within the frequency range of the second mode is shown in Fig. 9b. The comparison is very good around the maxima at 282 kHz. Apart from 282 kHz, the growth rates have more error. The relative error of the growth rates within the frequency range of the second mode is $\mathcal{O}(10^{-2})$. The growth rates are more sensitive to small error. Hence, the relative error of the growth rates appears to be more significant than the one of the normalized amplitudes of the pressure perturbations at wall. Both the comparisons imply that the results within the frequency range of the second mode for the current grid are reliable.

The freestream hotspot perturbations used in the current study have a Gaussian temperature profile in time. The frequency spectrum, which also has a Gaussian distribution, of the forcing disturbances is shown in Fig. 20. The freestream temperature perturbations have higher amplitudes when the frequency is lower and the amplitudes decrease with increasing frequency.

It is worth to notice that the small vertical magnitude in Fig. 20 is the Fourier transform (in the unit of per Hertz) of the initial disturbances in the freestream, which is not directly the relative wave amplitude. To obtain a wave amplitude in a given frequency range, we need to integrate the line in that figure along the frequency that is in

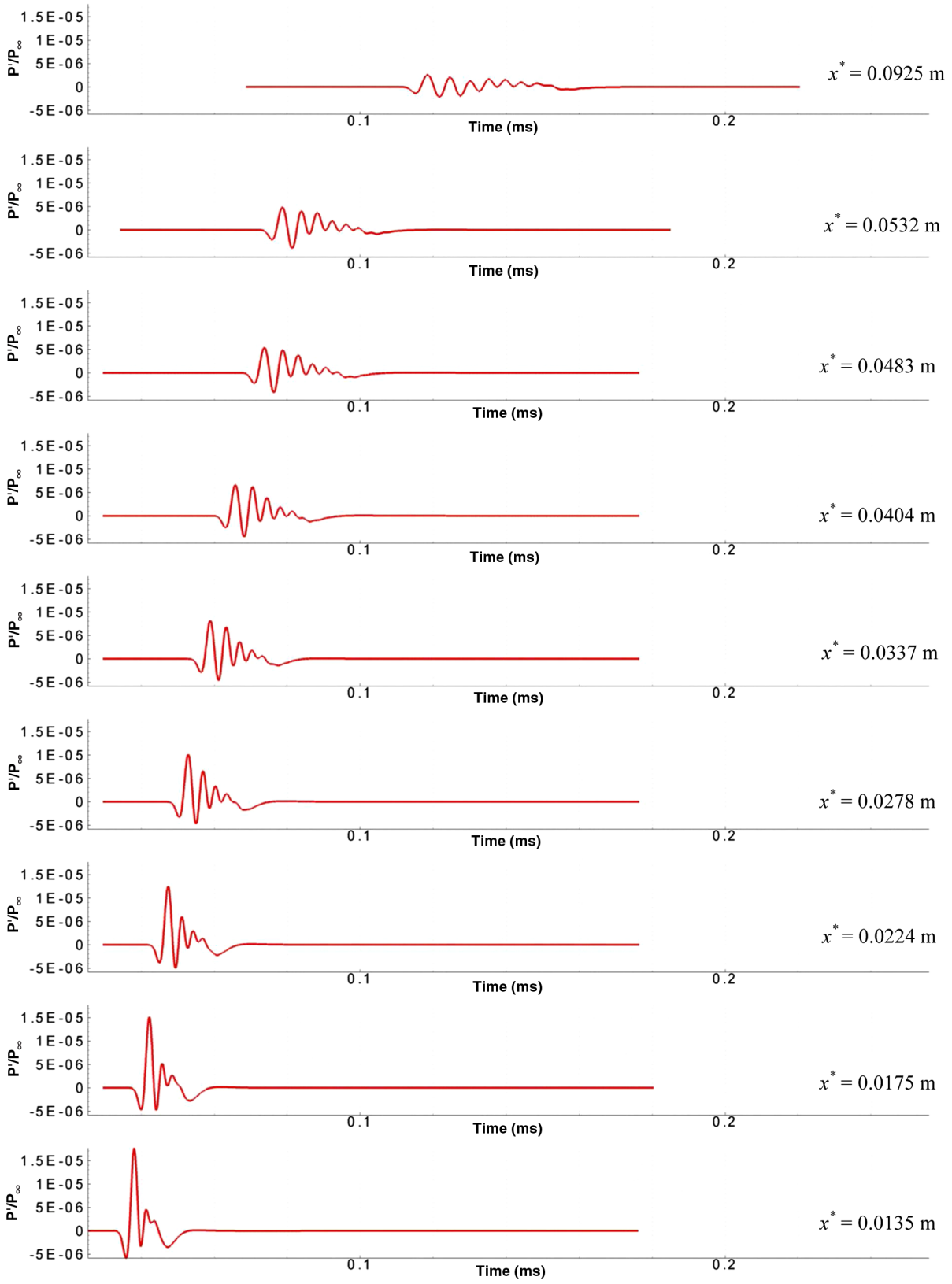

Fig. 17 Time-history traces of wall-pressure perturbations at various streamwise locations in upstream part of the cone.

the order of 100 kHz. As a result, the practical relative wave amplitudes in the simulation for the interesting range of up to 420 kHz are about 10^{-5} to 10^{-6}. We use double precision in the current computations with machine epsilon of approximately 10^{-16}. Both the disturbances in the freestream and behind the shock have small Fourier-transformed amplitudes with the frequencies below 420 kHz, but they are not yet close to the machine epsilon for a double-precision system.

It is shown in Fig. 20 that the amplitudes of the freestream forcing disturbances are not uniform at different frequencies. Hence, to reflect such frequency effects on the receptivity, it is necessary to normalize the amplitudes of the wall-pressure perturbations by those of the freestream forcing disturbances. Because the wall perturbations are pressure perturbations, whereas the freestream forcing disturbances are temperature disturbances, the normalization is defined by the following.

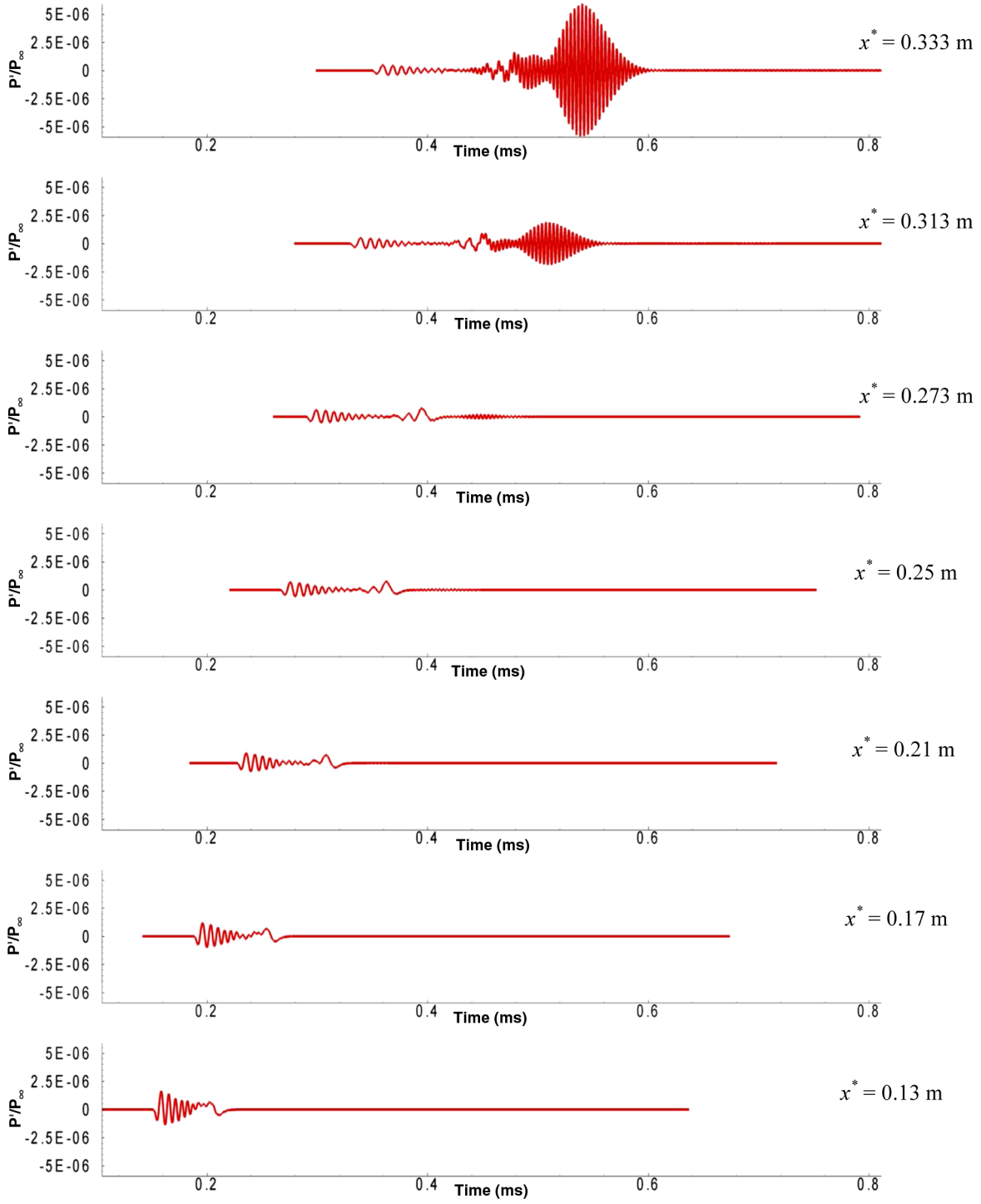

Fig. 18 Time-history traces of wall-pressure perturbations at various streamwise locations in downstream part of the cone.

Normalized amplitude:

$$\frac{|dP(F)/P_\infty|}{|dT_\infty(F)/T_\infty|} \tag{29}$$

where the dimensionless amplitude of the boundary-layer pressure perturbations is normalized by the one of the freestream temperature perturbations of the same frequency. This normalized amplitude is a more accurate description of the receptivity and instability growth.

The normalized amplitude frequency spectra of behind-shock acoustic waves and entropy waves in the nose region are shown in Figs. 21a and 21b. Both waves are generated by the combined interactions of the shock with the freestream hotspot perturbations and the reflected acoustic waves behind the shock. Each line represents the spectrum at a shock location that has a specific angle between the stagnation line in front of the cone nose and the line that connects the shock location and the origin. Because the maximum amplitude of the freestream hotspot perturbations is at the centerline, the maximum generated acoustic and entropy waves behind the shock appear on the stagnation line where the angle is 0. These generated waves decay at downstream shock locations in the nose region. The normalized amplitudes of the acoustic wave spectra decrease for frequencies beyond 240 kHz. Those of entropy waves increase at lower frequencies and reach a peak around 560 kHz. From Figs. 21a and 21b, it can be seen that the maximum relative strength to freestream perturbations for the pressure disturbances just behind the shock is about 45, which is much higher than the one (about 0.13) of the entropy disturbances. Therefore, after the hotspot/shock

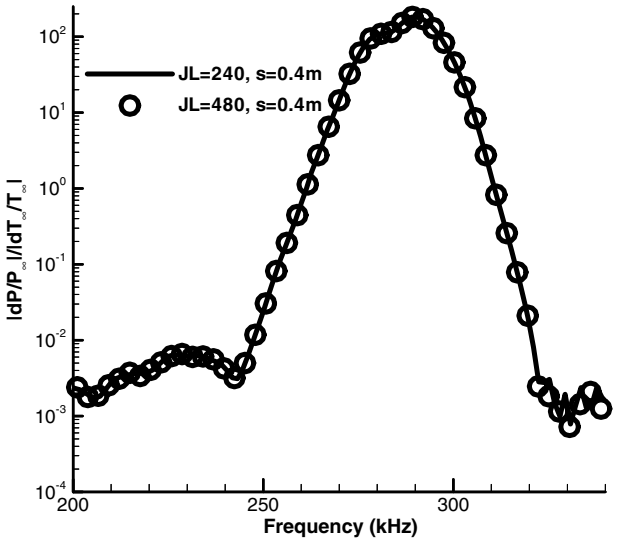

a)

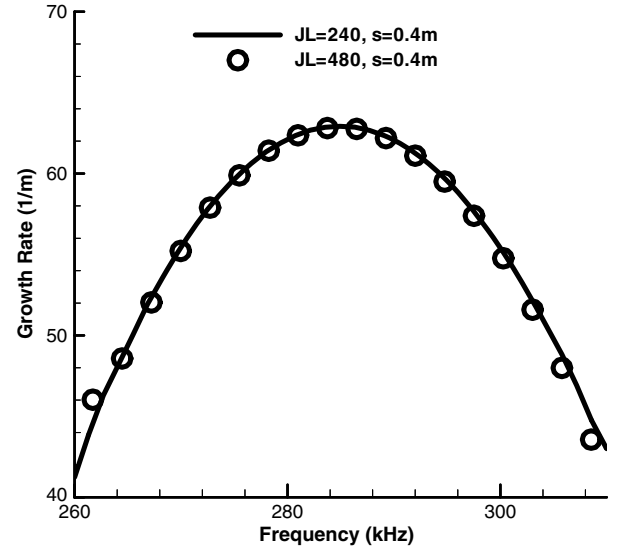

b)

Fig. 19 Comparisons of frequency spectrum of a) the normalized amplitude, and b) growth rate of pressure perturbations at the wall for two sets of grids.

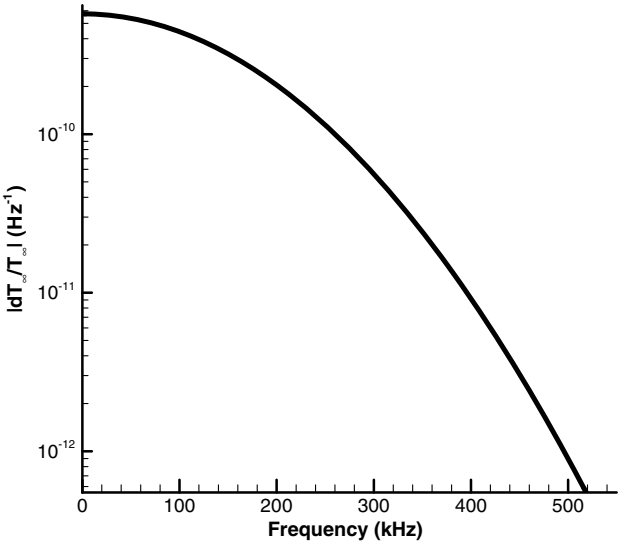

Fig. 20 Frequency spectrum of freestream temperature perturbations of the hotspot.

interaction in the nose region, acoustic waves are the largest disturbances generated.

Figure 22 shows the normalized frequency spectra in the flared region of the cone. In the figure, there is a large peak of spatial growth of amplitudes with the frequency ranging from about 240 to 320 kHz. This growing peak is the instability dominated by the second mode. The frequency corresponding to the maximum amplitude is about 290 kHz, and the frequency shift is insignificant. There is no significant shift expected because the boundary-layer thickness does not change significantly along the compression region of the cone. Such observation is discussed in Sec. VI.A. The frequency of the peak from the experiment, which is reported by Wheaton et al. [16] under similar flow conditions, is also 290 kHz. The weaker peak that is at the frequency range from 120 to 240 kHz decays spatially from $x^* = 0.13$ to 0.21 m. It is indeed likely to be the stable first mode. The oscillations in the spectra are caused by multimode wave modulations, which are complex physical process with a coexistence of many wave modes. Noticeably, no such oscillation appears over the peaks dominated by the Mack modes.

Because the boundary-layer receptivity is linear in the current study, the normalized amplitudes can be treated as independent of the shape function of the freestream forcing waves. The dimensionless amplitudes of the local disturbances at the wall can be obtained

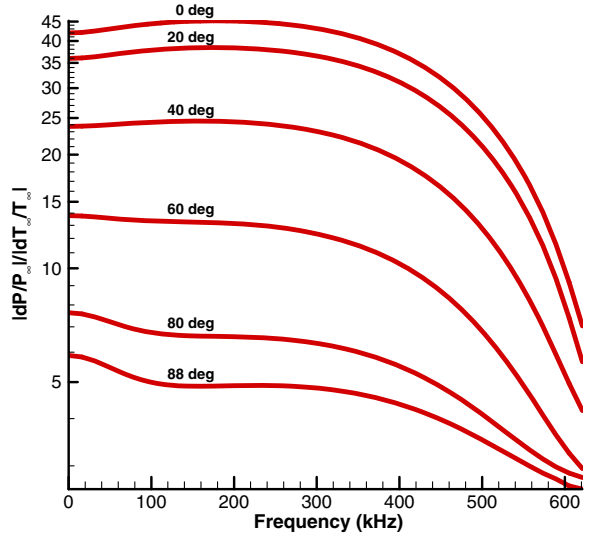

a)

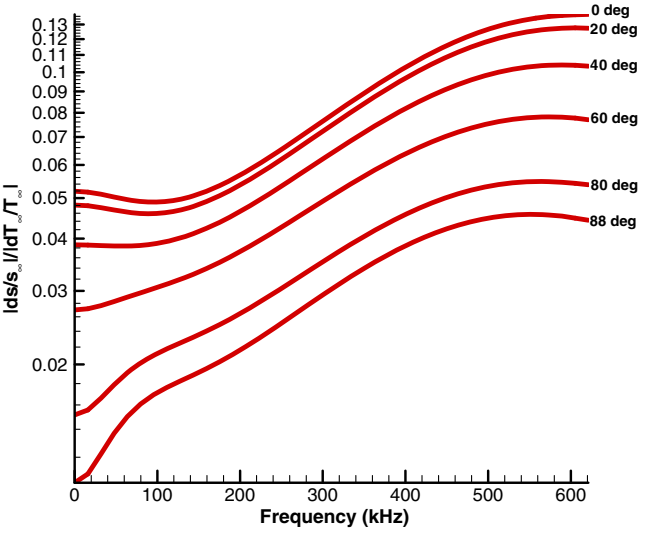

b)

Fig. 21 Frequency spectrum of normalized amplitudes of a) pressure perturbations, and b) entropy perturbations immediately behind the shock in the nose region.

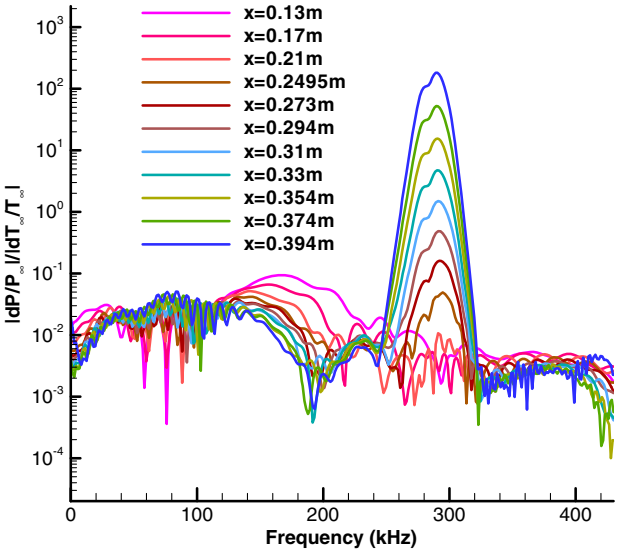

Fig. 22 Frequency spectra of the normalized pressure perturbations at the wall.

linearly by multiplying the dimensionless freestream forcing amplitude of a different shape function to the normalized amplitude at each frequency according to Eq. (29). Once the spectra of normalized amplitudes at all stations of a cone are obtained from a simulation, a database of receptivity to general forcing under the given geometry and flow conditions is then built. However, a different set of normalized amplitude spectra is needed for a different set of flow conditions and cone geometry.

The normalized amplitude is used to quantify the strength of boundary-layer disturbance growth relative to the freestream perturbations during the linear receptivity process. The waves that are transformed into the frequency domain become complex values; in other words, each wave component has a phase angle. Because the phase angle of each freestream perturbation component is different, the relative phase angles of the boundary-layer disturbances to the freestream one are used to describe the phase shift. The frequency spectrum of the relative phase angles at the end of the cone is shown in Fig. 23. The phase shift consistently increases as the frequency increases. The bumps are probably caused by the multimode wave modulations. Finally, by obtaining the relative phase angles in addition to the normalized amplitudes, one can reconstruct the actual waveform of the wall-pressure disturbances within the linear receptivity regime from the freestream entropy perturbations with different shape functions [25].

E. Boundary-Layer Receptivity Mechanism

After the frequency spectra are found, an investigation of the spatial modal evolution of the perturbations before the second-mode dominance is conducted. It is a crucial step to understand the receptivity mechanism. Figure 24 shows the spatial development of wall-pressure-perturbation amplitudes from the upstream region to the downstream region. In the plot, the five simulated second-mode sampling frequencies are the closest available to the five frequencies used in the LST study. These five frequencies start with high initial amplitudes where the hotspot just passes through the shock and the boundary-layer disturbances are excited in the upstream region. Then the perturbations decay while moving downstream. When they reach $s^* = 0.16$ m, they begin to grow exponentially downstream. The oscillatory features of the curves are the results of the modulation of multiple wave modes when there is no single dominant instability mode. This multimode modulation phenomenon is expected in the synchronization zone. They are commonly seen in many numerical studies [1,5,7–9,20]. They are not the spurious results of Fourier decomposition.

The following comparisons between the current simulated results and those from LST are aimed to quantitatively validate the current simulation. The validation is performed in the downstream region because it is more difficult to resolve the flow details there. Therefore, it is important to demonstrate that the solutions are well resolved there. The simulated growth rate is calculated by Eq. (15). The comparison between the numerically simulated spatial growth rates and those found from LST over the second-mode frequency range at four surface locations is shown in Fig. 25. At a fixed location, the LST and the current numerical simulation predict nearly the same peak frequency for the second-mode-dominated growth. However, the numerically simulated maximum growth rate is slightly higher than the one predicted by LST. Table 2 shows the comparison of the peak frequencies and growth rates between the simulation results and LST. The relative differences of the growth rates consistently decrease when the second mode becomes more dominant in the simulated disturbances downstream. The relative differences of the peak frequencies at all four locations are below 1%, which indicates a very good comparison between the frequencies of the maximum simulated growth rates and LST. The reason for the differences in growth rates to occur is because there are modulations due to the physical interaction between multiple modes, which cannot be decomposed by Fourier decomposition. Moreover, the nonparallel

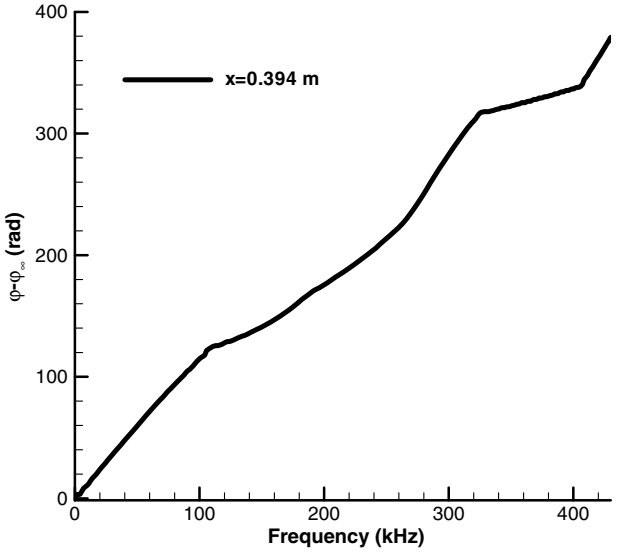

Fig. 23 Frequency spectrum of phase angle difference between the induced wall-pressure disturbances and the freestream temperature disturbances.

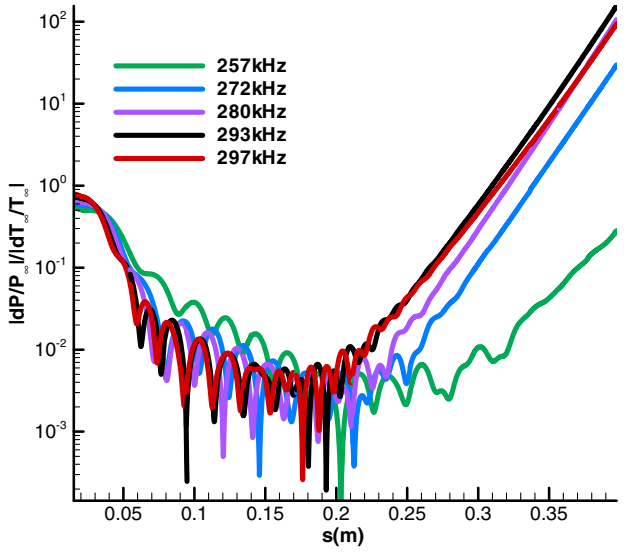

Fig. 24 Spatial development of numerically simulated wall-pressure perturbations for five sampling frequencies in the second-mode frequency range.

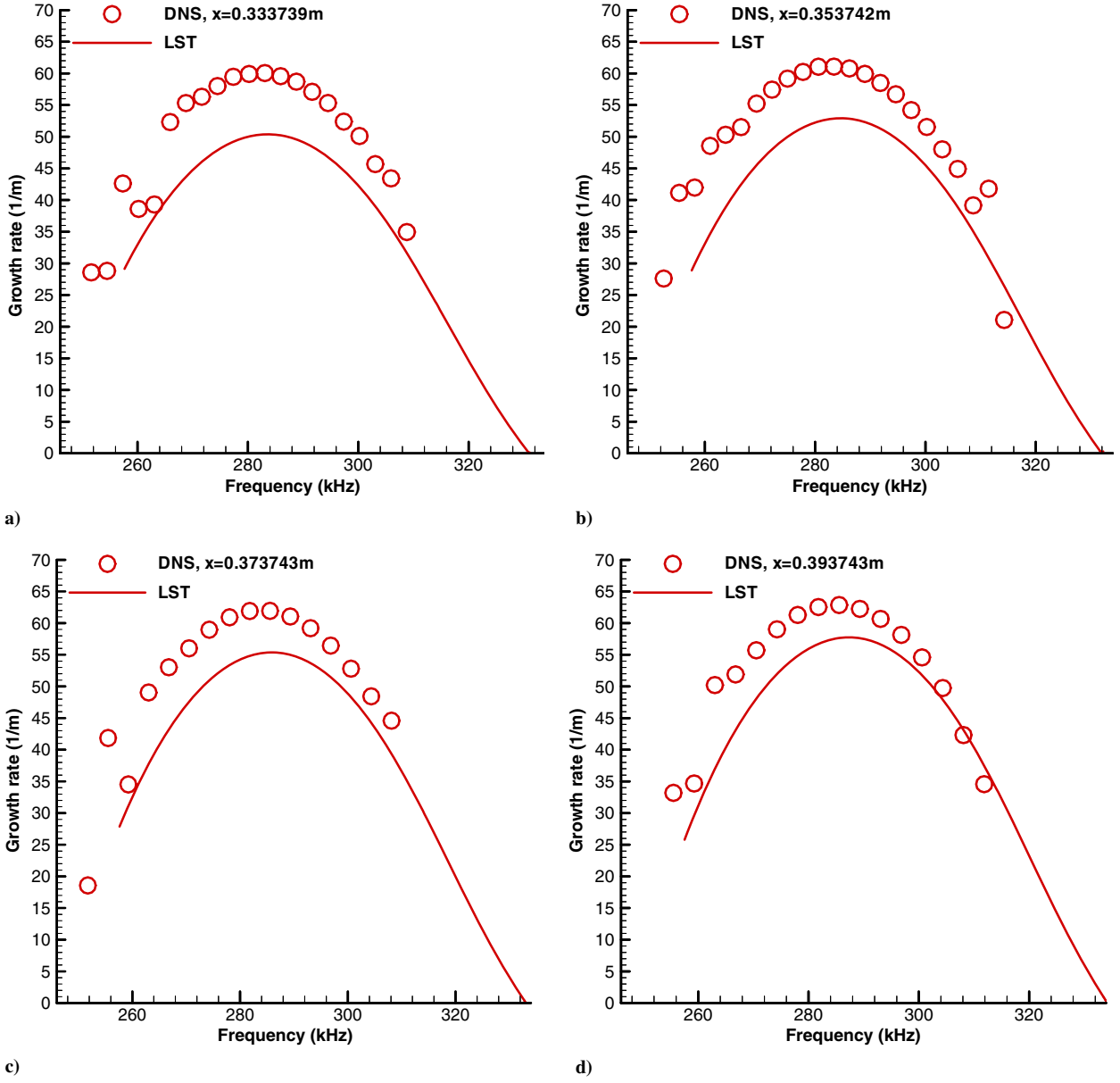

Fig. 25 Comparison of the growth rates between numerical simulation and LST as a function of frequency in the unstable second-mode region: a) $x^* = 0.333739$ m b) $x^* = 0.353742$ m, c) $x^* = 0.373743$ m, and d) $x^* = 0.393743$ m.

and surface curvature effects are not accounted for the current LST model.

The simulated dimensional wave number is calculated from Eq. (16). Figure 26 compares the frequency spectra of the wave numbers at the same four surface locations. The maximum relative differences between the two sets of wave numbers are 7.5% at $x^* = 0.33$ m, 5.2% at $x^* = 0.35$ m, 2.3% at $x^* = 0.37$ m, and below 1% at $x^* = 0.39$ m. The numerical wave numbers agree with those of the LST very well at the downstream location of $x^* = 0.39$ m.

Figure 27 shows an excellent agreement between the mode shapes of the current simulation and the LST with the most amplified second-mode sampling frequency of 293 kHz behind the synchronization point. Based on the reasonable agreements of the three comparisons, it is concluded that the numerical simulation successfully captures the linear second-mode development of the boundary-layer perturbations.

From the previous simulated data of perturbation amplitudes along the cone, we cannot determine the modal evolution in the boundary layer at different locations. Therefore, we have to compare the simulated results to the theoretical results to identify the dominant wave modes in the boundary layer with a fixed frequency. The frequency to be analyzed is the most amplified one (293 kHz) in the second-mode range. The simulated dimensionless phase speed is

Table 2 Comparison of growth rate spectra between the current simulation results and LST

x location, m	Relative difference of maximum growth rates	LST peak frequency, kHz	Simulated peak frequency, kHz
0.33	16%	284	282
0.35	13%	284.5	283.5
0.37	11%	286	284
0.39	8%	287.5	286

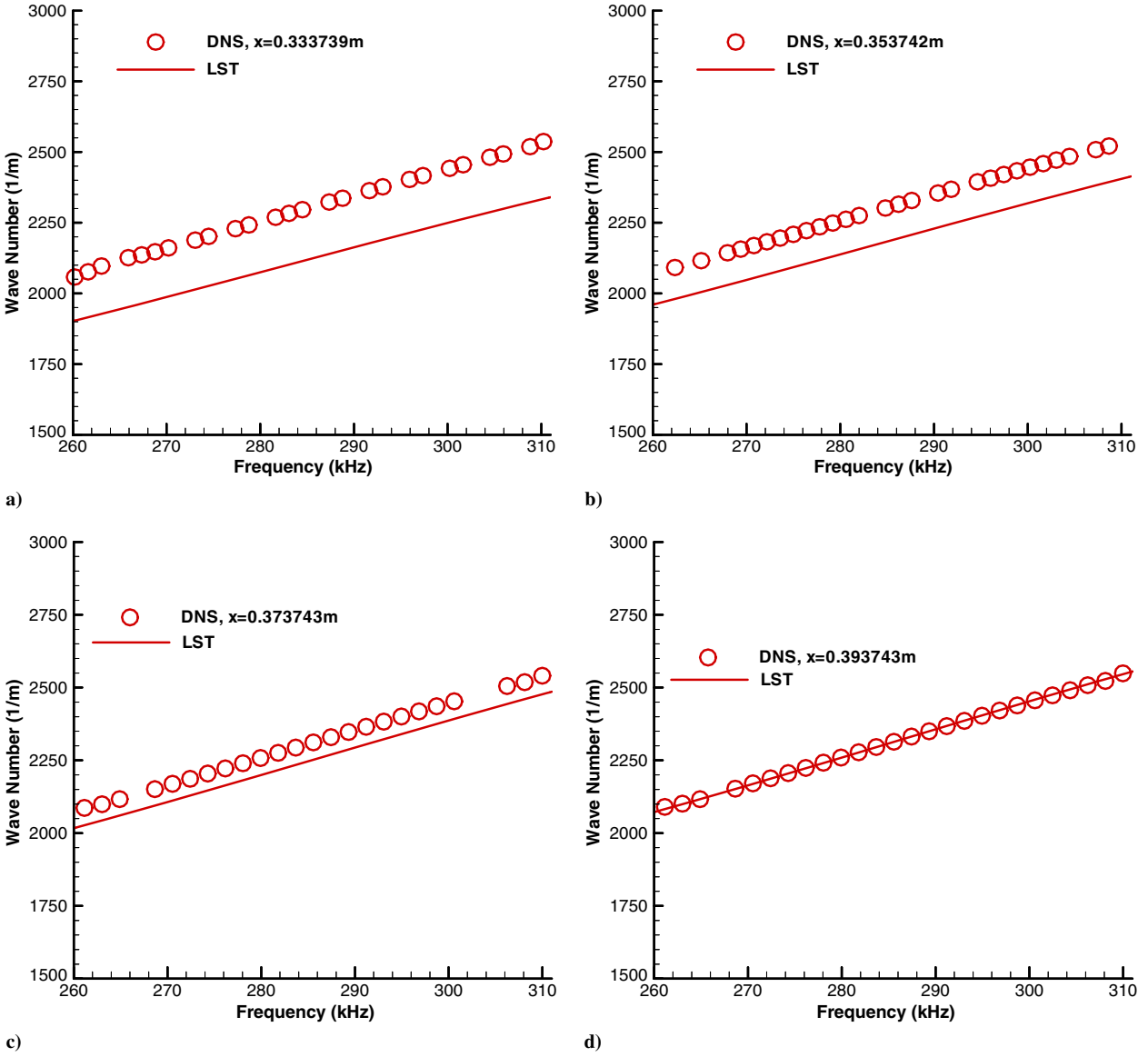

Fig. 26 Comparison of the wave numbers between numerical simulation and LST as a function of frequency in the unstable second-mode region: a) $x^* = 0.333739$ m b) $x^* = 0.353742$ m, c) $x^* = 0.373743$ m, and d) $x^* = 0.393743$ m.

computed by Eqs. (16), (23), and (25). The comparison between the simulated phase speed and the phase speed obtained from LST is shown in Fig. 28. The three horizontal lines are the dimensionless phase speeds of fast acoustic, slow acoustic, and entropy/vorticity waves determined using freestream flow conditions in front of the bow shock. As a result, they only serve as qualitative references to show the existence of the three wave modes. The actual phase speeds depend on local nonconstant flow conditions. Figure 28 shows a trend of the phase speed of the simulated disturbances decreasing from the phase speed of the fast acoustic wave in the nose region. The simulated phase speed closely matches the LST predicted mode F with very slight oscillations until $s^* = 0.04$ m. The comparison shows that the disturbances are likely to be initially excited in the boundary layer by the fast acoustic waves near the nose. The comparison also shows that mode F is relatively strong in the boundary-layer disturbances before $s^* = 0.04$ m. The oscillations begin after the phase speed of the waves reaches the one of entropy/vorticity waves, and it rises up to the phase speed of fast acoustic waves between $0.04 < s^* < 0.2$ m. The modulation between all the wave modes causes the strong oscillations in that region. More specifically, there are several disturbance modes existing in the simulated boundary-layer disturbances, whereas the LST assumes clean boundary-layer waves with pure mode F and mode S. As a result, the modulations of the simulated results reflect the coexistence

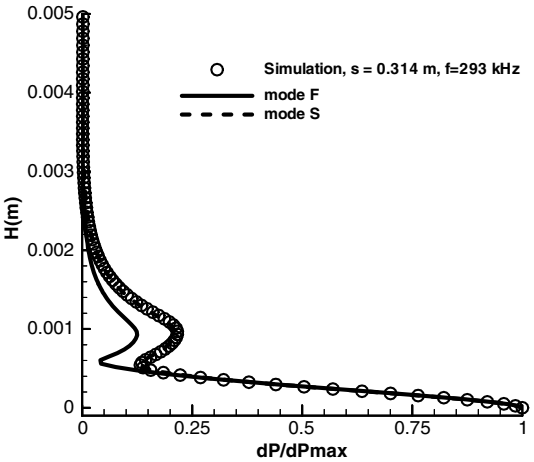

Fig. 27 Comparison of wall-normal mode shapes of pressure perturbations between the simulation and LST with the frequency of 293 kHz at $s^* = 0.314$ m.

of other modes. Moreover, all the modes are relatively strong in the modulation region. The same phenomenon was also discussed by Zhong and Ma [5] and Ma and Zhong [8,9].

In Fig. 28, the phase speed in the modulation region is close to the fast acoustic waves. It indicates that the boundary-layer disturbances contain a significant proportion of fast acoustic waves in that region relative to other modes. As the waves propagate further downstream, the phase speed decreases and becomes almost the same as the mode S behind the synchronization point of mode S and mode F at $s^* = 0.16$ m. This observation indicates that the dominance of mode S in the boundary-layer disturbances begins after the synchronization between mode S and mode F.

In Fedorov et al. [21,32], a branch point is where both the real and imaginary parts of the phase speed are equal for mode F and mode S. The second-mode instability is excited downstream from the branch point. The branch point, however, does not exist in most practical flows with a real x axis (or Reynolds numbers) only, except for a very specific disturbance frequency with a very cold wall. Instead, the branch point appears along complex Reynolds number with a nonzero imaginary part. In the case of practical flow, mode F and mode S have resonance interaction when the real part of the wave number and frequency are the same near the branch point, even though the growth rates are different. Therefore, we define the synchronization point, which is also the resonant point, between mode F and mode S as the point where the real parts of the phase speed are equal for mode F and mode S. Zhong and Ma [5] and Ma and Zhong [8,9] have shown that this synchronization point plays an important role in receptivity process.

In Figs. 28–30, there is a break in the phase speeds, wave numbers, and growth rates of mode F around $s^* = 0.09$ m. It is due to the fact that the eigenvalue of the discrete mode F merges into the entropy/vorticity spectrum and reappears while moving downstream before reaching the synchronization point. As a result, the eigenvalue of mode F is interrupted by the entropy/vorticity spectrum. Because the actual phase speed of entropy/vorticity waves depends on local flow conditions, the break appears below the freestream phase speed of entropy/vorticity waves in Fig. 28. This break is typical for hypersonic flow over a cone. It is similar to the one shown in Fig. 11 in Zhong and Ma [5] for a Mach 8 flow over a cone. Again, it is a result of mode F crossing the continuous spectrum as demonstrated in Fig. 10 of Zhong and Ma.

The simulated dimensionless wave number is calculated by Eqs. (16) and (23). The wave-number comparison between numerical simulation and LST is shown in Fig. 29. The plot confirms the observations that are made by the preceding phase-speed comparison; the induced waves contain relatively strong mode F before the disturbances reach $s^* = 0.04$ m, and modulation between all the waves occurs between $0.04 < s^* < 0.2$ m. The wave numbers of mode F and mode S cross each other around $s^* = 0.16$ m; hence, the synchronization point is located there. Though the wave numbers of mode F and mode S seem to be very close, as shown in Fig. 29, they are in fact different in the region behind the synchronization point. The differences can be more clearly seen in the nondimensional phase-speed comparison in Fig. 28. Therefore, there is only the synchronization point, not a synchronization line or a long region.

The stability of the boundary-layer disturbances at different locations is determined by their growth rates. The simulated growth rate is calculated by Eq. (15). The comparison between the simulated growth rate and the one obtained from LST is shown in Fig. 30. There are oscillations in the simulated growth rate as a result of multimode wave modulations. The simulated growth rate eventually converges to the unstable growth rate of mode S behind $s^* \approx 0.2$ m. Both growth rates of the simulation and mode S compare very well downstream. The plot also shows that mode F is stable everywhere, whereas mode S is stable before $s^* = 0.11$ m, and it becomes unstable behind this location. These observations indicate that the unstable second mode is related to mode S, and the induced disturbances become second-mode-dominated behind the synchronization point ($s^* = 0.16$ m), which is the similar conclusion made in the preceding discussion of the phase-speed plot in Fig. 28. In addition, even though the unstable region of mode S begins earlier than the synchronization point, the disturbances of 293 kHz in Fig. 24 grow only behind $s^* = 0.16$ m. From this observation, we further conclude that the synchronization of mode F and mode S leads to the

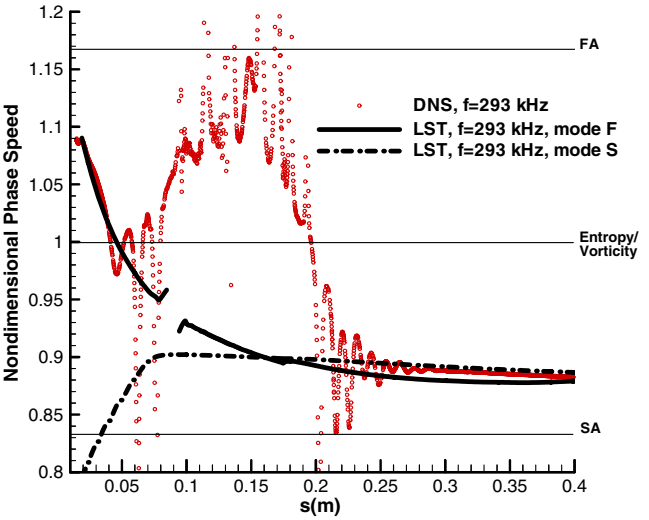

Fig. 28 Comparison of the streamwise phase speeds of the simulated wall disturbances with those of mode F and mode S by LST with the frequency of 293 kHz.

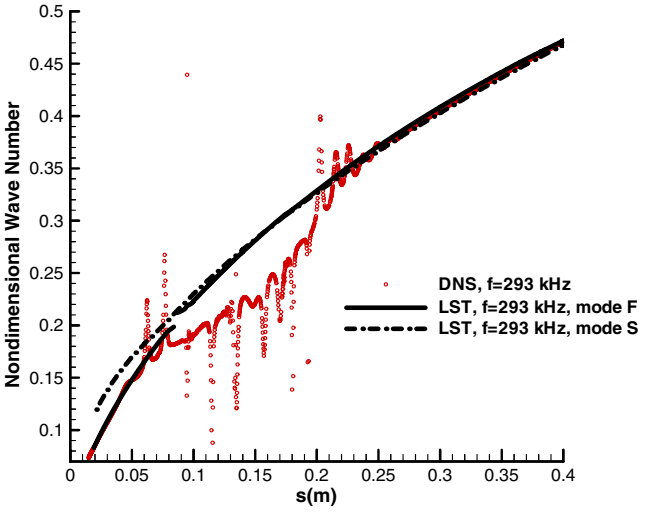

Fig. 29 Comparison of the streamwise wave numbers of the simulated wall disturbances with those of mode F and mode S by LST with the frequency of 293 kHz.

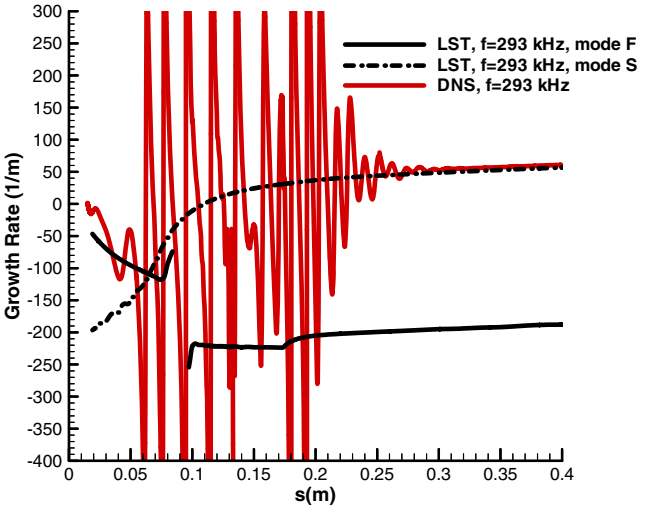

Fig. 30 Comparison of the growth rates of the simulated wall-pressure disturbances with those of mode F and mode S by LST with the frequency of 293 kHz.

dominance of boundary-layer disturbances by the growing second mode. Zhong and Ma [5] and Ma and Zhong [8,9] have also shown that even though the modulation region exists, the resonance interactions of mode F and mode S at the synchronization point still cause the dominance of the second mode in the boundary-layer disturbances.

To confirm the previous identification of modal evolution in the induced boundary-layer disturbances, we compare the boundary-layer mode shapes between simulation and LST at different locations. These are shown in Figs. 27 and 31a–31e. At $s^* = 0.03$ m, where the modulations begin to appear upstream, the simulated mode shape is very close to mode F. This comparison shows that the boundary-layer disturbances have relatively strong mode F in the upstream region of multimode wave modulation. While moving further downstream to $s^* = 0.0687$ m and $s^* = 0.1083$ m, which are near the locations of both ends of the break in the phase speed of mode F, the simulated mode shape begin to deviate from mode F. It does not approach mode S at this point. These observations show that neither mode F nor mode S can stand out among all the wave components in the induced disturbances when the eigenvalue of mode F is in the vicinity of the

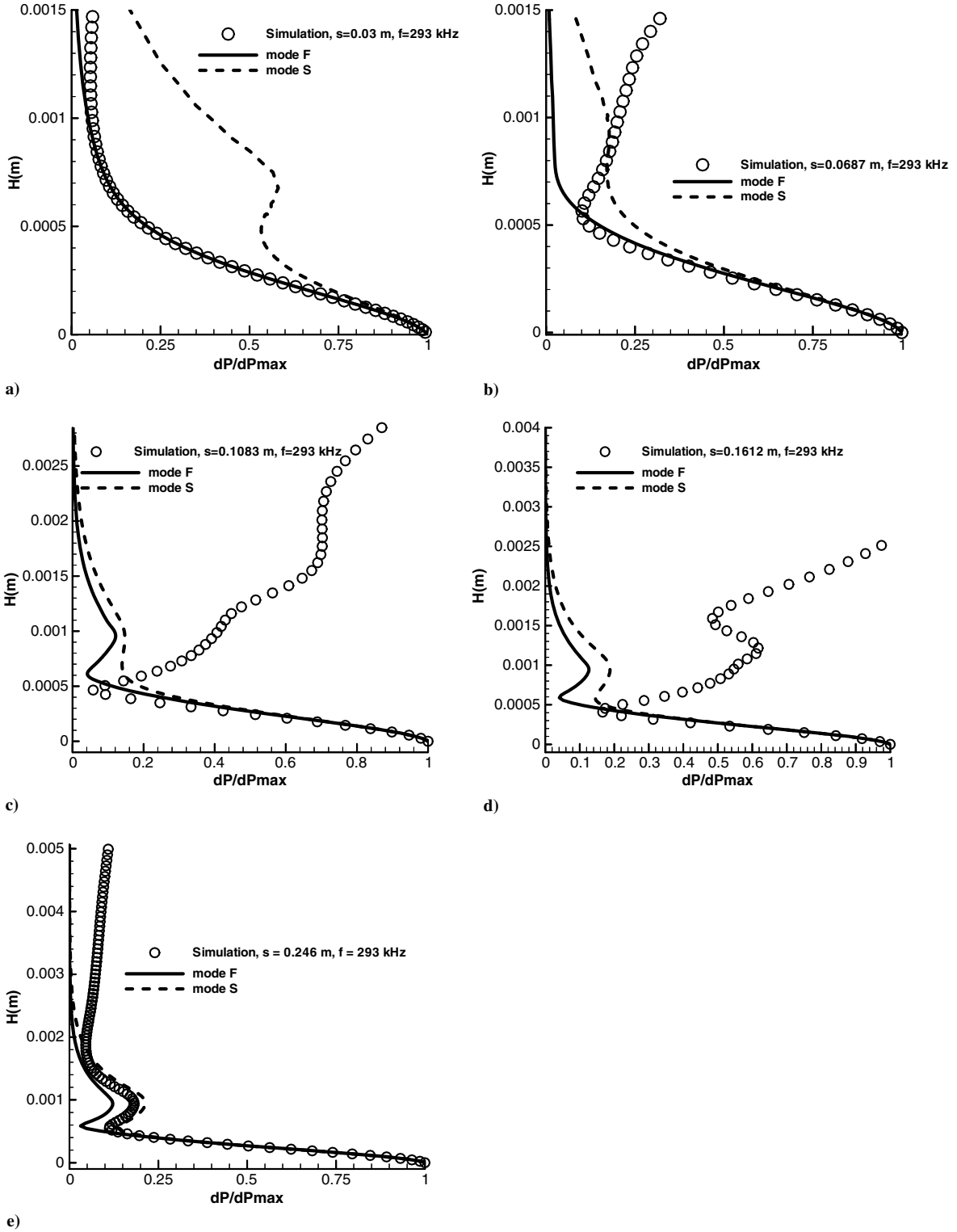

Fig. 31 Comparisons of wall-normal mode shapes of pressure perturbations between the simulation and LST with the frequency of 293 kHz at various locations.

entropy/vorticity spectrum. The differences outside the boundary layer between the simulated mode shape and the LST reflect the existence of freestream transient forcing outside the boundary layer in the simulated results, while the LST is free of freestream forcing. When the boundary-layer disturbances reach the vicinity of synchronization point at $s^* = 0.1612$ m, the simulated mode shape begins to approach mode S. When the disturbances move further downstream from the synchronization point to $s^* = 0.246$ m and $s^* = 0.314$ m, the comparisons shows that the simulated mode shape converges to mode S. Especially at $s^* = 0.314$ m, the simulated mode shape compares very well to mode S. The comparisons at the last two locations behind the synchronization point show that the mode S has strong and rapid domination to the boundary-layer disturbances after they pass through the synchronization point. These observations of the mode shapes confirm the receptivity path obtained in the phase speed, wave number, and growth rate comparisons.

The receptivity mechanism with the second-mode frequency analyzed in this section agrees with the receptivity to freestream acoustic waves over a blunt cone, which is reported in Zhong and Ma [5], and the receptivity to freestream entropy waves over a flat plate in Ma and Zhong [9]. However, this is essentially different from the receptivity over a flat plate reported by Fedorov et al. [20], where, in their case of freestream temperature spot, mode S is excited after the slow acoustic waves (which are generated by the spot-shock interaction) penetrate the boundary layer.

VII. Conclusions

In the current study, numerical simulations for both the steady base flow and the freestream hotspot perturbed flow over a compression cone have been conducted. The behavior of the boundary-layer disturbances throughout the receptivity process has also been investigated. In addition to this, the receptivity mechanism was also studied, and a receptivity database for the compression cone under the Mach 6 flow conditions was built. Specifically, one set of response amplitudes and phase angles in the Fourier frequency space was stored. Even though this is a challenging task, it is feasible with today's supercomputers as described in Lei and Zhong [25]. Such a database can be used to reconstruct the boundary-layer disturbances in the linear regime under general freestream entropy forcing, which provides the initial conditions for the study of nonlinear boundary-layer disturbance.

The study of the boundary-layer receptivity mechanism that leads to second-mode dominant growth is carried out by comparing the simulated results to LST. The disturbances are likely to be initially excited in the boundary layer by fast acoustic waves nearby the nose. Then, mode F appears to be relatively strong in the boundary-layer disturbances in the upstream region. The unstable mode S, which is the second mode, is excited by the synchronization of mode F and mode S. Moreover, such synchronization leads to the dominance of boundary-layer disturbances by the growing second mode.

In conclusion from all the results, introducing the interaction between freestream hotspot and bow shock is an effective way to trigger second-mode instability in a hypersonic boundary layer, which could eventually lead to laminar–turbulent transition downstream of a cone. In addition, the receptivity mechanism to freestream entropy spot for hypersonic flow over a blunt cone is similar to that for hypersonic flow over the flat plat with entropy waves of a single discrete frequency in the freestream. However, even though both studies show a similar mechanism, it is not an automatic extension of previous studies because the effects of bow shock and entropy layer were not included in the case of a flat plate.

Similarly, it was found that the mechanism of receptivity to freestream entropy perturbations over a cone is essentially different from the case of a hypersonic flow over a flat plate with freestream temperature spots. These findings show that the receptivity mechanism over different geometries can be significantly different. On the other hand, the receptivity mechanism is found to be similar to the one for acoustic waves over a blunt cone. Such findings are not reported in a previous study.

Acknowledgments

This work was sponsored by the U.S. Air Force Office of Scientific Research/NASA National Center for Hypersonic Research in Laminar–Turbulent Transition and by the U.S. Air Force Office of Scientific Research, under grant FA9550-07-1-0414, monitored by John Schmisseur. The views and conclusions contained herein are those of the authors and should not be interpreted as necessarily representing the official policies or endorsements either expressed or implied, of the U.S. Air Force Office of Scientific Research or the U.S. Government. The authors of this paper appreciate Steven P. Schneider at Purdue University and his group for providing the data and information of their compression cone and other wind-tunnel experiments.

References

[1] Zhong, X., "Receptivity of Mach 6 Flow over a Flared Cone to Freestream Disturbance," *42nd AIAA Aerospace Sciences Meeting and Exhibit*, AIAA Paper 2004-0253, Jan. 2004.

[2] Mack, L. M., "Boundary Layer Linear Stability Theory," AGARD Rept. 709, 1984.

[3] Kovasznay, L. S. G., "Turbulence in Supersonic Flow," *Journal of the Aeronautical Sciences*, Vol. 20, No. 10, 1953, pp. 657–682. doi:10.2514/8.2793

[4] McKenzie, J. F., and Westphal, K. O., "Interaction of Linear Waves with Oblique Shock Waves," *Physics of Fluids*, Vol. 11, No. 11, 1968, pp. 2350–2362. doi:10.1063/1.1691825

[5] Zhong, X., and Ma, Y., "Boundary-Layer Receptivity of Mach 7.99 Flow over a Blunt Cone to Free-Stream Acoustic Waves," *Journal of Fluid Mechanics*, Vol. 556, June 2006, pp. 55–103. doi:10.1017/S0022112006009293

[6] Balakumar, P., and Kegerise, M. A., "Receptivity of Hypersonic Boundary Layers over Straight and Flared Cones," *48th AIAA Aerospace Sciences Meeting*, AIAA Paper 2010-1065, Jan. 2010.

[7] Balakumar, P., and Kegerise, M. A., "Receptivity of Hypersonic Boundary Layers to Acoustic and Vortical Disturbances," *49th AIAA Aerospace Sciences Meeting*, AIAA Paper 2011-371, Jan. 2011.

[8] Ma, Y., and Zhong, X., "Receptivity of a Supersonic Boundary Layer over a Flat Plate. Part 2. Receptivity to Free-Stream Sound," *Journal of Fluid Mechanics*, Vol. 488, July 2003, pp. 79–121. doi:10.1017/S0022112003004786

[9] Ma, Y., and Zhong, X., "Receptivity of a Supersonic Boundary Layer over a Flat Plate. Part 3. Effects of Different Types of Free-Stream Disturbances," *Journal of Fluid Mechanics*, Vol. 532, June 2005, pp. 63–109. doi:10.1017/S0022112005003836

[10] Fedorov, V. A., "Receptivity of a High-Speed Boundary Layer to Acoustic Disturbances," *Journal of Fluid Mechanics*, Vol. 491, Sept. 2003, pp. 101–129. doi:10.1017/S0022112003005263

[11] Maslov, A. A., Shiplyuk, A. N., Sidorenko, A. A., and Arnal, D., "Leading-Edge Receptivity of a Hypersonic Boundary Layer on a Flat Plate," *Journal of Fluid Mechanics*, Vol. 426, Jan. 2001, pp. 73–94. doi:10.1017/S0022112000002147

[12] Schmisseur, J. D., Collicott, S. H., and Schneider, S. P., "Laser-Generated Localized Freestream Perturbations in Supersonic and Hypersonic Flows," *AIAA Journal*, Vol. 38, No. 4, 2000, pp. 666–671. doi:10.2514/2.1008

[13] Schmisseur, J. D., "Receptivity of the Boundary Layer on a Mach 4 Elliptic Cone to Laser-Generated Localized Free Stream Perturbations," Ph.D. Dissertation, School of Aeronautics and Astronautics, Purdue Univ., West Lafayette, IN, Dec. 1997.

[14] Salyer, T. R., Collicott, S. H., and Schneider, S. P., "Characterizing Laser-Generated Hot Spots for Receptivity Studies," *AIAA Journal*, Vol. 44, No. 12, 2006, pp. 2871–2878. doi:10.2514/1.13023

[15] Salyer, T. R., "Laser Differential Interferometry for Supersonic Blunt Body Receptivity Experiments," Ph.D. Dissertation, School of Aeronautics and Astronautics, Purdue Univ., West Lafayette, IN, 2002.

[16] Wheaton, B. M., Juliano, T. J., Berridge, D. C., Chou, A., Gilbert, P. L., Casper, K. M., Steen, L. E., and Schneider, S. P., "Instability and Transition Measurements in the Mach-6 Quiet Tunnel," *39th AIAA Fluid Dynamics Conference*, AIAA Paper 2009-3559, June 2009.

[17] Johnson, H. B., and Candler, G. V., "Analysis of Laminar–Turbulent Transition in Hypersonic Flight Using PSE-Chem," *36th AIAA Fluid Dynamics Conference and Exhibit*, AIAA Paper 2006-3057, June 2006.

[18] Chou, A., Wheaton, B. M., Ward, C. A. C., Gilbert, P. L., Steen, L. E., and Schneider, S. P., "Instability and Transition Research in a Mach-6 Quiet Tunnel," *49th AIAA Aerospace Sciences Meeting*, AIAA Paper 2011-0283, Jan. 2011.

[19] Fedorov, V. A., Ryzhov, A. A., and Soudakov, G. V., "Numerical and Theoretical Modeling of Supersonic Boundary-Layer Receptivity to Temperature Spottiness," *41st AIAA Fluid Dynamics Conference and Exhibit*, AIAA Paper 2011-3077, June 2011.

[20] Fedorov, V. A., Ryzhov, A. A., Soudakov, G. V., and Utyuzhnikov, S. V., "Receptivity of a High-Speed Boundary Layer to Temperature Spottiness," *Journal of Fluid Mechanics*, Vol. 722, May 2013, pp. 533–553.
doi:10.1017/jfm.2013.111

[21] Fedorov, V. A., and Khokhlov, A. P., "Prehistory of Instability in a Hypersonic Boundary Layer," *Theoretical and Computational Fluid Dynamics*, Vol. 14, No. 6, 2001, pp. 359–375.
doi:10.1007/s001620100038

[22] Fedorov, A., and Tumin, A., "High-Speed Boundary Layer Instability: Old Terminology and a New Framework," *AIAA Journal*, Vol. 49, No. 8, 2011, pp. 1647–1657.
doi:10.2514/1.J050835

[23] Heitmann, D., and Radespiel, R., "Simulation of the Interaction of a Laser Generated Shock Wave with a Hypersonic Conical Boundary Layer," *41st AIAA Fluid Dynamics Conference and Exhibit*, AIAA Paper 2011-3875, June 2011.

[24] Heitmann, D., Radespiel, R., and Knauss, H., "Experimental Study of Mach 6 Boundary Layer Response to Laser Generated Disturbances," *41st AIAA Fluid Dynamics Conference and Exhibit*, AIAA Paper 2011-3876, June 2011.

[25] Lei, J., and Zhong, X., "Numerical Simulation of Freestream Waves Receptivity and Breakdown in Mach 6 Flow over Cone," *43rd AIAA Fluid Dynamics Conference*, AIAA Paper 2013-2741, 2013.

[26] Chou, A., "Characterization of Laser-Generated Perturbations and Instability Measurements on a Flared Cone," M.S. Thesis, School of Aeronautics and Astronautics, Purdue Univ., West Lafayette, IN, 2010.

[27] Zhong, X., "High-Order Finite-Difference Schemes for Numerical Simulation of Hypersonic Boundary-Layer Transition," *Journal of Computational Physics*, Vol. 144, No. 2, 1998, pp. 662–709.
doi:10.1006/jcph.1998.6010

[28] Lei, J., and Zhong, X., "Linear Stability Analysis of Nose Bluntness Effects on Hypersonic Boundary Layer Transition," *48th AIAA Aerospace Sciences Meeting*, AIAA Paper 2010-0898, Jan. 2010.

[29] Malik, M. R., "Numerical Method for Hypersonic Boundary Layer Stability," *Journal of Computational Physics*, Vol. 86, No. 2, 1990, pp. 376–413.
doi:10.1016/0021-9991(90)90106-B

[30] Stetson, K. F., Thompson, E. R., Donaldson, J. C., and Siler, L. G., "Laminar Boundary Layer Stability Experiments on a Cone at Mach 8, Part 2: Blunt Cone," *22nd AIAA Aerospace Sciences Meeting*, AIAA Paper 1984-0006, Jan. 1984.

[31] Huang, Y., and Zhong, X., "Numerical Study of Boundary-Layer Receptivity on Blunt Compression-Cones in Mach-6 Flow with Localized Freestream Hot-Spot Perturbations," *RTO Applied Vehicle Technology Panel (AVT) Specialists' Meeting on Hypersonic Laminar-Turbulent Transition*, NATO Science and Technology Organization Paper 20, April 2012.

[32] Fedorov, V. A., and Khokhlov, A. P., "Receptivity of Hypersonic Boundary Layer to Wall Disturbances," *Theoretical and Computational Fluid Dynamics*, Vol. 15, No. 4, 2002, pp. 231–254.
doi:10.1007/s001620100052

M. Choudhari
Associate Editor